# Volatiles of the active Mayotte volcanic chain: STA & EGA-MS analysis of volcanic products

Thivet Simon [1, *], Hess Kai-Uwe [1], Dingwell Donald B. [1], Berthod Carole [2, 3], Gurioli Lucia [4], Di Muro Andrea [5], Lacombe Tristan [4], Komorowski Jean-Christophe [2]

[1] Ludwig-Maximilians-Universität, Department of Earth and Environmental Sciences, 80333 Munich, Germany
[2] Université Paris Cité, Institut de Physique du Globe de Paris, CNRS, 75005 Paris, France
[3] Observatoire Volcanologique et Sismologique de la Guadeloupe, Institut de physique du globe de Paris, 97113 Gourbeyre, France
[4] Laboratoire Magmas et Volcans, Université Clermont Auvergne, CNRS, IRD, OPGC, 63178 Aubière, France
[5] Laboratoire de Géologie de Lyon : Terre, Planètes, Environnement, UMR 5276, CNRS, Ecole Normale Supérieure de Lyon, Université Claude Bernard Lyon 1, 69622 Villeurbanne, France

* Corresponding author : Simon Thivet, email address : simon.thivet@lmu.de

**Abstract :**

In July 2018, a large (ca. 6.55 km3), deep (ca. 2.5 to 3.3 km b.s.l) submarine eruption started ca. 50 km east of Mayotte Island. Samples of fresh basanitic lava rims were collected by dredging, at various times and locations from the newly formed Fani Maoré Edifice (FME). The logistical response to this extraordinary event also enabled the dredging of shallow (ca. 1.2 to 1.6 km below sea level, b.s.l.), fresh phonolitic lava and bomb rims in the so-called Horse-Shoe Area (HSA), ca. 15 km east of Mayotte. Better-known subaerial counterparts of Holocene age, have also been sampled in the La Vigie Maar (LVM) phonolitic deposits (Petite-Terre, Mayotte Island), for comparison with submarine samples. These samples belong to a single volcanic chain that extends from LVM to FME passing through HSA. A novel combination of Simultaneous Thermal Analysis (STA), which involves Differential Scanning Calorimetry (DSC), Thermal Gravimetry Analysis (TGA), and Evolved Gas Analysis conducted by Mass Spectrometry (EGA-MS), enable a reconstruction of the volatile distributions and compositions (H2O, CO2, and SO2) of these samples. Calorimetric and degassing profiles of controlled heating runs reveal different volatile reservoirs distributed as a function of sample textures and compositions, which have been further investigated by Scanning Electron Microscopy (SEM), Electron Probe Micro-Analysis (EPMA), and Raman spectroscopy. A linear correlation observed between the TGA and H2O-EGA-MS signal intensities also enables the quantification of adsorbed-external vs. dissolved-magmatic H2O contents of the studied samples. The novel application of this approach to volcanic products is thus confirmed as a reliable method to determine volatile characteristics in a wide range of samples, yielding a quantitative description of volatile behavior within the associated magmatic systems and eruptions.

**Highlights**

► Mayotte volcanic chain is formed by submarine and subaerial alkaline volcanic products. ► STA combined with EGA-MS technique allows the quantification of adsorbed vs. magmatic $H_2O$. ► Rock texture and composition control volatiles distribution and behavior. ► Hydrostatic pressure delays magmatic $H_2O$ exsolution in the submarine products. ► Magmatic $CO_2$ exsolves at high magmatic pressures, forming CO2-rich bubbles and fluids.

**Keywords** : Basanite, Evolved gas analysis by mass spectrometry, Magma, Phonolite, Simultaneous thermal analysis

## 1. Introduction

Volatiles in magmas are of crucial importance in processes ranging from magma generation and transport to volcanic and passive degassing at the Earth's surface (e.g., Aiuppa et al., 2008; Wallace et al., 2015; Thivet et al., 2021). $H_2O$ is commonly the dominant volatile

species in magmatic melts, playing a central role in magmatic processes during magma transport and directly influencing eruptive dynamics (e.g., Cashman, 2004; McIntosh et al., 2014; Cassidy et al., 2018). $CO_2$ and $SO_2$ are dissolved in magmatic melts at lower concentrations. Each of these volatile species exsolves in a distinct manner from the ascending and crystallizing magma, with the vast majority of volatile contents being degassed in subaerial volcanic eruptions involving decompression to atmospheric pressure (e.g., Newman and Lowenstern 2002; Moore, 2008; Di Muro et al., 2016). In contrast, the eruption depths of submarine lavas yield significant hydrostatic pressures at which deep submarine lavas erupted on the ocean floor are emplaced. Due to the pressure dependence of volatile solubilities, the products of such deep submarine eruptions contain much higher volatile contents (e.g., Moore, 1970; Ligi et al., 2005; White et al., 2015). The fact that a comparatively small fraction of volatiles is exsolved under submarine conditions results in different magmatic state (porosity, crystallinity, and permeability), and derivative properties and behavior (viscosity, fragmentation intensity and eruptive style) (e.g., Zhang, 2009; Chavrit et al., 2012; Colombier et al., 2021).

Upon decompression, magmatic melt degassing is generally accompanied by crystallization (e.g., Lipman et al., 1985; Szramek et al., 2006; Applegarth et al., 2013) which leads to microlite and nanolite populations (e.g., Sharp et al., 1996; Mujin et al., 2017; Matsumoto and Geshi, 2021). These processes can lead to severe shifts in certain magma properties (i.e., buoyancy and viscosity), system degassing (i.e., from closed to open or vice versa) and ultimately thereby impact eruptive styles of volcanic eruptions at the Earth´s surface (e.g., Cáceres et al., 2020; Di Genova et al., 2020; Thivet et al., 2020a).

Upon efficient eruptive quenching (i.e., relatively fast cooling rates) some magmatic melts cool to the glass transition temperature ($T_G$) interval with little or no crystallization and transform to glass (Zanotto and Mauro, 2017). One of the physical expressions of $T_G$ interval is the viscous to brittle transition, where magma explosivity and fragmentation are induced, and where clast sintering can occur during volcanic eruptions (e.g., Dingwell and Webb, 1989; Dingwell, 1996; Cashman and Scheu, 2015; Scheu and Dingwell, 2022).

Thus, textural (i.e., crystallinity and porosity), chemical (i.e., vesicle, glassy matrix, and crystal compositions), and physical (i.e., $T_G$) characteristics of erupted volcanic products are critical sources of information on magmatic processes occurring before and during an eruption. Here, we characterize a set of volcanic samples (Fig. 1) among different contexts of extrusion (submarine vs. subaerial products), eruptive style (effusive vs explosive dynamics), and composition (basanitic vs. phonolitic) from a single, active volcanic chain located in the Comoros archipelago area, stretching east for 50 km from Petite-Terre Island, Mayotte (e.g., Feuillet et al., 2021; Tzevahirtzian et al., 2021; Berthod et al., 2021b). In total, 17 volcanic samples have been investigated in the search for variations in volatile distributions and contents as a function of sample textures, compositions, and syn-eruptive confining pressures. Our analytical approach combines traditional Electron Probe Micro-Analysis (EPMA), Scanning Electron Microscopy (SEM), and Raman spectroscopy (e.g., Di Muro et al., 2015; Gurioli et al., 2018; Berthod et al., 2021a), with Simultaneous Thermal Analysis (STA) and Evolved Gas Analysis conducted by Mass Spectrometry (EGA-MS), whereby STA refers to the simultaneous application of Differential Scanning Calorimetry (DSC; e.g., Potuzak et al., 2008; Nichols et al., 2009; Helo et al., 2013) and Thermal Gravimetry Analysis (TGA; e.g., Leonelli et al., 2013; Song et al., 2014; Biren et al., 2020) to the same sample in a single instrument. EGA-MS (e.g., Schöps et al., 2005; Heide et al., 2008; McAdam et al., 2019) is performed with an independent device connected to the STA apparatus. STA and EGA-MS analysis simultaneously provides thermal, mass, and volatile degassing evolutions of samples upon heating and under a controlled atmosphere. We conclude in the present study that this innovative approach represents an accessible and a fast method to obtain complementary insights to traditional textural and geochemical analysis of volcanic products. More specifically,

it represents an efficient way to determine volatile distributions and contents, delivering reliable information to better understand volatile degassing and associated processes in magmatic systems.

## 2. Geological background

### 2.1. Mayotte active volcanic chain

This study focuses on volcanic samples collected in the Mayotte volcanic chain (Fig. 1a), the easternmost island of the Comoros archipelago otherwise composed of three main islands (from west to east: Grande Comore, Mohéli, Anjouan, and Mayotte) in the northern part of the Mozambique Channel. Recent studies of this system focusing on tectonics and volcanic edifice morphology have led to the suggestion that this volcanic archipelago is strongly influenced by regional lithospheric fractures associated with strike-slip faulting linked to the Lwandle-Somali plate boundary (Famin et al., 2020; Tzevahirtzian et al., 2021). Magnetic data are consistent with the presence of oceanic crust in this area (Coffin and Rabinowitz, 1987). Volcanism at Mayotte stretches back ca. 28 Ma (Masquelet et al., 2022). Its accessible products yield a wide range of alkaline compositions from basanite-tephrite to phonolite and exhibit a wide range of volcanic deposits (Bachèlery and Hémond, 2016; Michon, 2016). Morphological considerations have been used to infer that the main volcanism migrated in time progressively northward and westward, forming Mayotte, Anjouan, Mohéli, and finally Grande Comore Island (Michon, 2016; Tzevahirtzian et al., 2021; Thinon et al., in revision), with the last of these four islands hosting Karthala volcano, which is the most active emerged volcano of the archipelago (Bachèlery et al., 2016; Liuzzo et al., 2021; Thivet et al., 2022), although Holocene volcanic activity has also been recorded on Anjouan Island (Quidelleur et al., 2022).

In May 2018, an unprecedented and intense seismic crisis associated with an unambiguous ground deflation, started offshore east of Mayotte Island (Cesca et al., 2020; Lemoine et al., 2020). These events have been correlated with the drainage of a large (> 10 km$^3$) and deep (37-48 km below sea level, b.s.l.) mantle-hosted magma reservoir generating magma migration towards the seafloor (Berthod et al., 2021a; Foix et al., 2021; Lavayssière et al., 2022). This led to the largest submarine eruption monitored to date with a total volume of ca. 6.55 km$^3$ and a dense rock equivalence of ca. 4.8 km$^3$ (REVOSIMA, 2022). Modelling of the onset of this event yields dates between 18 June and 3 July (according to Cesca et al., 2020 and Lemoine et al., 2020, respectively) and lasted at least until early 2021 as eruptive activity was detected in January 2021 by the MAYOBS 17 campaign; Thinon et al., 2021). From the beginning of the eruption and for a maximum duration of 320 to 336 days, the average minimum volume flow rate was ca. 172 to 181 m$^3$/s, which represents the highest estimated lava emission flux since the 1783 historical eruption of Laki, Iceland (REVOSIMA, 2022). The eruption occurred ca. 50 km east of Mayotte Island on the ca. 3.3 km deep seafloor and formed the ca. 800 m tall Fani Maoré Edifice (FME) with associated outlying lava flows (Fig. 1b). This new volcano complemented a pre-existing alignment of submarine volcanic edifices, forming the Mayotte volcanic chain that extends westwards until Petite-Terre Island and the northeast of Grande-Terre Island, Mayotte (Feuillet et al., 2021).

Several volcanic edifices sitting nearby the remarkable horseshoe-shaped submarine volcanic feature known as the Horse-Shoe Area (HSA, Fig. 1a) are characterized by well-marked, non-eroded morphological features and unaltered deposits which is suggestive of their recent age, probably from Holocene.

Also, the presence of tephra layers in the lagoon sediments between Petite-Terre and Grande-Terre Islands suggests that volcanic activity on Petite-Terre Island, including La Vigie Maar (LVM, Fig. 1a), occurred less than 7000 years ago (Zinke et al., 2003; 2005).

Thus, the eruption of Fani Maoré constitutes a remarkable illustration that major volcanism can suddenly resume after repose periods of undetermined time length in this system. It further demonstrates a lack of any clear pattern of volcanic activity migration in the Mayotte active volcanic chain and more largely on the construction of the islands of the Comoros archipelago, despite their apparent morphological evolution.

## 2.2. Sampling sites

Investigated samples were collected from three previously described areas (FME, HSA and LVM), which belong to the same volcanic alignment (Fig. 1c). Rims of lava or bombs (between 1 and 5 cm thick) were selected for the present study as they should represent the state of rapidly quenched products with a high potential thereby for preserving the parental texture and composition of the magma. Due to their inferred slower cooling, lava flow and bomb interiors are, in contrast, potentially susceptible to a more protracted phase of crystallization and volatile loss (e.g., Wright et al., 2007; Heide et al., 2008; Schipper et al., 2010). A detailed sample list is provided in the supplementary material (Table S1). Below, the sampling is described.

The samples from the FME, dredged between 2.8 and 3.3 km b.s.l. in three different MAYOBS campaigns, provide good coverage of the 2018-2019 eruptive period (Berthod et al., 2022b). DR01 (MAYOBS 1, Feuillet, 2019), DR10 and DR12 (MAYOBS 4, Fouquet and Feuillet, 2019) lavas were erupted before May 2019 during a first cone-building phase (phase 1), whereas DR08 (MAYOBS 2, Jorry, 2019) and DR11 (MAYOBS 4) lavas were erupted during a second phase characterized by peripheral lava outflowing (phase 2), in June and July 2019, respectively. Petrological and geochemical variations of the eruptive products, Berthod et al. (2021a) reveal that these two distinct phases were representative of two different magmatic pathways during the eruption: during phase 1 (from May 2018 to May 2019) the eruption was fed by a direct rise of magma from the deep mantle reservoir, whereas during phase 2 (from May to August 2019) a shallower, sub-crustal (ca. 17 km deep), smaller, tephri-phonolitic magma reservoir (identified by passive seismic tomography, Foix et al., 2021), was intersected and sampled by the less evolved initial upwelling magma. Finally, the magma pathway shifted once more within the crust resulting in a new eruption site located 6 km northwest of the main edifice. Ten lava rim samples investigated in the present study were selected from phase 1 (6 samples) and phase 2 (4 samples), respectively.

The samples from the HSA were dredged between 1.2 and 1.6 km b.s.l.. Two lava rims from DR02 (MAYOBS 1) and DR07 (MAYOBS 2), as well as two bomb rims from DR17 (MAYOBS 15, Rinnert et al., 2020) have been selected for the present study. These samples (of unknown age at the time of writing) are unaltered and the two bomb rims come from the same fragment, from dense and vesicular portions, respectively.

Finally, bombs from LVM subaerial deposits (of unknown age at the time of writing) were collected in July 2021. Three bomb rims have been selected for the present study. Two of these samples come from the same fragment, characterized by an intercalation of pumiceous and dense layers, which were separated for independent analysis.

## 3. Laboratory methods

The samples, previously dried for 48 hours at 60 °C, were first manually broken into coarse chips (≤ 1 cm). For each sample, the chips were split into two sub-samples, (i) for polished sections for EPMA, SEM, and Raman spectroscopy, and (ii) further crushed (≤ 2 mm) for STA and EGA-MS. Care was taken to ensure that both split fractions were homogeneous and similar in appearance. Data acquired in the present study are compiled in the supplementary material of this paper (File S1, Tables S2, S3, S4, S5, and S6).

### 3.1. Electron Probe Micro-Analysis (EPMA), Scanning Electron Microscopy (SEM), and Raman spectroscopy analyses

For EPMA and SEM analyses, polished sections were carbon coated (10 nm) using a Leica Sputter Coater EM ACE600. Groundmass compositions were measured using a Cameca SX100 EPMA with an acceleration voltage of 15 kV, and a probe current intensity of 8 nA with 10 s counting times and a defocused (10 μm) beam. Routine standards (i.e., diopside, rutile, orthoclase, hematite, pyroxmangite, albite, xenotime) were used for elemental calibration. Five groundmass analyses were acquired for each analyzed sample to check sample homogeneity and analysis reproducibility.

Textural description and quantification were achieved via 2D Back-Scattered Electron (BSE) images using a Hitachi SU5000 Field-Emission SEM with an acceleration voltage of 10 kV. Energy-Dispersive Spectroscopy (EDS) was also employed, with an acceleration voltage of 20 kV to acquire chemical maps and *in-situ* spectra and ease the identification of crystalline phases. Where feasible, vesicle and crystal contents were estimated from representative sample portions (i.e., from x60 to x800 magnified SEM-BSE images depending on the vesicle and crystal size of the samples). Crystal content estimations provided in the present study are porosity-corrected.

Raman spectra were acquired on the groundmass from 50 to 4000 cm$^{-1}$ Raman shift, using a Jobin Yvon XPlora One spectrometer coupled with an Olympus microscope. The instrument was calibrated using a silicon standard. Instrumental settings consisted of 1800 grooves/mm grating density, a confocal hole of 300 μm, and a slit of 200 μm with an exposure time of 60 s repeated 3 times. A x100 magnification was used during the acquisitions, with a laser excitation wavelength of 532 nm and an applied filter of 50 %. Band intensities and peak shifts were determined after applying the Long's correction on the raw spectra and subtraction of piecewise linear baselines. Between two and three spectra were acquired and averaged for each analyzed sample.

### 3.2. Simultaneous thermal analysis (STA) and evolved gas analysis by mass spectrometry (EGA-MS)

A Mettler Toledo TGA/DSC 3+ apparatus was used for the STA (Fig. 2a). The sensor of this device is located in a high-temperature furnace and features a twin crucible holder. This consists of a twin platinum-rhodium disk that is fitted into an alumina frame. The right disk is the sample position: for each analysis, each crushed sample (mass between 15 and 25 mg) was placed into an $Al_2O_3$ crucible covered by an $Al_2O_3$ perforated lid, to avoid any potential sample explosion, dispersion, and contamination into the furnace. $Al_2O_3$ crucibles are the most convenient ones for repeated STA and EGA-MS analysis because of their relatively affordable cost, as well as their stable chemical and thermal properties at high temperatures, allowing accurate measurements of both sample mass and temperature. The left disk is the reference position, which is occupied by an empty $Al_2O_3$ crucible covered by an $Al_2O_3$ perforated lid. An R-type thermocouple (± 2 °C) positioned under the reference side disk measured the reference temperature. An additional R-type thermocouple (± 2 °C) measured the temperature difference between the sample and the reference side, producing a differential thermal signal, which is directly proportional to the calorimetric raw data, measured as the heat flow in mW. The sensor is also connected to a highly sensitive microbalance (± 0.1 μg), providing sample mass change for each analysis. STA was systematically corrected by reproducible baseline measurements performed with empty crucibles at both sample and reference sides.

A fused quartz capillary (internal diameter of 10 μm) enclosed in a heated transfer line connects the STA device to a ThermoStar Pfeiffer Vacuum GSD 320 EGA-MS (Fig. 2a), which

simultaneously identifies the targeted volatile species released during each analysis. This EGA-MS is equipped with an inlet heater that heats up the transfer line to 150 °C to avoid gas condensation within the capillary. It is also equipped with an integrated vacuum pump that creates a $10^{-9}$ bar environment to collect the gases from the STA furnace through the capillary, allowing a relatively immediate response and synchronous analysis of the released volatile species (delay of about ca. 1 sec between the STA and the EGA-MS signals). The EGA-MS consists of four cylindrical rods (quadrupole) set parallel to each other. The collected gases are ionized by a filament and separated in the rod system based on their mass-to-charge (m/z) ratio and on the stability of their trajectories in the oscillating electric fields that are applied to the rods. The ions are then electrically detected with a Continuous Secondary Electron Multiplier (C-SEM) detector (sensitivity of 1 ppm).

The specific analytic protocol that was run for each sample is detailed in Fig. 2b. Before each analysis, the STA furnace was systematically purged at room temperature (RT) and pressure, with a 25 min-long 120 mL/min Argon (Ar) flow, followed by a 20 min-long nominal 40 mL/min Ar flow in order to remove air and stabilize a baseline of gas concentration in the furnace. Next, each sample was heated from 40 °C (which was the maximum RT) to 1300 °C with a heating rate of 25 °C/min. Finally, each sample was cooled down to RT at a rate of 25 °C/min. Each analysis lasted ca. 160 min, resulting in a completely melted and re-solidified sample, adhering to the crucible which were thus not re-used. The Ar purging flow (Ar used is Ar 4.8 for spectrometry with a guaranteed purity of 99.998 %), which enables the conduction of analyses under relatively dry and reduced conditions, allows to measure simultaneously the release of $H_2O$ (m/z = 18), $CO_2$ (m/z = 44), and $SO_2$ (m/z = 64), all of which do not interfere with the signal of Ar (m/z = 40).

## 4. Results and interpretations

### 4.1. Geochemical and textural characteristics of the studied samples

#### 4.1.1. Groundmass chemical compositions

Groundmass compositions (Figs. 3a and 3b) show a clear chemical evolution from the FME phase 1 (mostly basanitic with a few trachy-basaltic) and FME phase 2 (mostly basanitic with a few phono-tephritic) samples to HSA and LVM (mainly phonolitic with a few trachytic) samples. Note that FME samples are classified as basanite rather than tephrite based on a normative olivine content > 10 % (Berthod et al., 2021a). This chemical trend is part of the moderately silica-undersaturated chemical evolution, the so-called "Karthala trend", which is widely observed in the Comorian system and reflects fractional crystallization of olivine + clinopyroxene + feldspar (e.g., Class et al., 1998; Bachèlery and Hémond, 2016; Berthod et al., 2021b). The slight increase of both alkalis and silica from FME phase 1 to phase 2 samples is a reflection of the differentiation trend towards tephri-phonolitic magma during phase 2, identified by Berthod et al. (2021a).

A spatio-temporal geochemical trend can be identified from these samples, whereby the less evolved FME basanitic lavas are the most easterly and recent samples of the volcanic chain, whereas the more evolved HSA and LVM phonolitic samples are older and more westerly, closer to the main and highly populated island of Mayotte (Fig. 1). We note however that Berthod et al. (2021b) have also demonstrated the presence of basanitic lavas in the Horse-Shoe Area (Fig. 3a). These geochemical variations presumably reflect the presence of an active, complex, and regionally-distributed plumbing system below the volcanic chain, favoring variable rates of fractional crystallization of primitive mafic magmas (Berthod et al., 2021b). We note that the geochemical data of the Comoros archipelago (and especially for the Mayotte volcanic chain) compiled by (Berthod et al., 2021b, Foix et al., 2021) highlight a geochemical

gap between the basanite and phonolite, suggesting that either the availability and/or the eruptability of intermediate phono-tephrite and tephri-phonolite magmas is low compared with that of the basanitic and phonolitic magmas.

Raman spectroscopy (Fig. 3c) reveals that the glassy groundmasses from all investigated FME samples are nanolite-bearing (cf. Sharp et al., 1996). Well-identified peaks possessing Raman shifts from 632 to 677 $cm^{-1}$ are inferred to reflect the presence of nanolites of one or more iron-bearing phases in the FME groundmasses (e.g., Di Genova et al., 2017, 2020; Cáceres et al., 2021), which are absent in the HSA and LVM ones. Total iron content ($FeO_t$, in wt.%) of the groundmasses (Fig. 3b), as well as both the silicate area band (LW, 200 to 1300 $cm^{-1}$) and the $H_2O$ area band (HW, 2700 to 3900 $cm^{-1}$) of the corrected Raman spectra, were determined in order to estimate the $H_2O$ content ($H_2O_{Raman}$, in wt.%) of the studied glasses (Fig. 3c), following the Di Genova et al. (2017) model: $H_2O_{Raman} = (HW/LW) \times (0.096 \times FeO_t + 0.663)$. We note that such estimations of $H_2O_{Raman}$ contents for the FME nanolite-bearing glasses (ranging between 0.6 and 1.1 wt.%) should be considered as minimum estimates because of the presence of the iron-bearing nanolites. Di Genova et al. (2017) showed that the HW areas of nanolite-bearing samples are lower than expected for a given $H_2O$ content, likely due to the presence of nanolites decreasing the analyzed hydrous glass volume. The nanolite-bearing nature of the FME lava groundmasses also induces heterogeneity and noise in the Raman spectra, especially at the HW band. Broad and noisy bands observed at ca. 3550 $cm^{-1}$ are related to molecular water, and narrow and intense peaks at ca. 3720 $cm^{-1}$ are most likely related to hydroxyl groups, (also taken into account in the $H_2O_{Raman}$ estimations). These minimum concentrations are nevertheless consistent with those measured by Berthod et al. (2021a) in the crystal-hosted melt inclusions of the FME lavas ($H_2O_{Raman} \geq 2.3$ wt.% for phase 1 melt inclusions coming from the ca. 37-48 km deep mantle magma reservoir; $H_2O_{Raman} \geq 1.2$ wt.% for phase 2 melt inclusions coming from the ca. 17 km deep sub-crustal magma reservoir). In contrast, Raman spectra obtained on HSA and LVM nanolite-free glasses are free of bias, enabling the calculation of accurate $H_2O_{Raman}$ contents for HSA glassy groundmasses from lavas (0.9 wt.%) and bombs (1.2 wt.%), as well as for LVM bomb glassy groundmasses (0.1-0.2 wt.%). No carbon/carbonate nor sulfur/sulfide/sulfate signatures were observed in the Raman spectra.

### 4.1.2. Textural characteristics of the FME samples

FME lavas have a low content (ca. 5 vol.%) of large (> 0.4 mm in length) xenoliths, xenocrysts and phenocrysts (Berthod et al., 2021a). Samples from FME lava rims are generally free of such large crystalline phases. They exhibit nonetheless complex textural features (Figs. 4a and 4b) consisting of subhedral to skeletal micro-phenocrysts (30 to 200 μm), acicular to dendritic microlites (1 to 30 μm) and nanolites (< 1 μm). The micro-phenocrysts include forsterite-rich olivines and Fe- and Ti-rich oxides (ilmenites and titanomagnetites), some of which exhibit melt and fluid inclusions (Figs. 4a and 4b, image 1). Based on crystal habits, shapes, compositions, as well as melt- and fluid-inclusion compositions, this crystal population has been interpreted by Berthod et al. (2021a) to have formed during the rapid magma ascent and decompression in the upper conduit (< 1 kbar). The microlite population is composed of Fe- and Ti-rich oxides (ilmenites and titanomagnetites), biotites, clinopyroxenes, apatites, and olivines (Figs. 4a and 4b, image 1). High magnification SEM-BSE images confirm that all investigated FME samples are nanolite-bearing, with the occurrence of equidimensional Fe-bearing nanolites (as suggested by Raman analyses) and further unidentified tabular and acicular nanolite phases (Figs. 4a and 4b, images 2 and 3). Textural features are interpreted to mean that microlite and nanolite growth probably occurred during eruptive quenching (c.f., Zhou et al., 2000; Giuliani et al., 2020). This interpretation is also supported by the occurrence of rare, thin (< 150 μm), translucent, glassy rims, which are observable in some FME samples.

Unfortunately, these portions were too thin and rare on the investigated dredged samples to be isolated for laboratory analysis. Thus, in comparison to hyper-quenched submarine glasses that exhibit efficient eruptive quenching (> 3000 °C/min, Potuzak et al., 2008), we infer that the studied FME lava samples reflect relatively inefficient eruptive quenching (< 100 °C/min) perhaps due to a high mean eruptive flux of lava (ca. 180 $m^3$/s) during the first year of the eruption (Feuillet et al., 2021) that subdued the thermal cooling of the lava mass via contact with seawater. Because of the occurrence of these quenching microlites and nanolites, crystal content estimation for the FME samples is given as a range: overall SEM-BSE image observations, taking into account phenocrysts and micro-phenocrysts (ca. 5 vol.%), as well as microlites and nanolites (between 20 and 45 vol.% depending on the sample and on image analysis parameters), provide an approximate and broad crystal content estimation between 25 and 50 vol.%. We also note that all the investigated FME samples show widespread nanoscale chemical heterogeneities interpreted as melt immiscibility (c.f. Veksler et al., 2007; Honour et al., 2019; Schuller, 2021), as shown in Figs. 4a and 4b, image 2. Microscale immiscible FeS droplets either included in olivine and titanomagnetite crystals or directly in the groundmass are also observed in these products (Fig. 4b, image 3), as already mentioned by Berthod et al., (2021a).

Berthod et al. (2021a) highlight that samples from FME phase 1 have slightly higher vesicle contents (35 vol.% on average) than FME phase 2 samples (25 vol.% on average). The DR12_05_01 sample from FME phase 1 exhibits the highest vesicle content and higher vesicle number density of the investigated samples, with a main vesicle population < 500 μm in diameter. These vesicularity values are in the typical range for alkaline and mafic submarine products (e.g., Kurz et al., 1983; Hekinian et al., 2000; Jones et al., 2020), suggesting that a non-negligible amount of volatiles has degassed from the pre-eruptive melt and during the magma decompression in closed-system degassing (where exsolved bubbles remain in equilibrium with the melt). As reflected by the "popping" behavior upon dredging and crushing of samples, as well as by BSE-SEM observations, most of the vesicles that are initially observed in the submarine FME lavas are isolated in the groundmasses and have kept their original magmatic gas content. Unambiguous observations of $CO_2$-, $CH_4$- and $H_2$-rich fluid emissions from the seafloor located in the HSA structure, corresponding to the central core of the active trans-crustal magmatic plumbing system (Feuillet et al., 2021, Liuzzo et al., 2021; Foix et al., 2021; REVOSIMA, 2022) suggest that volatile degassing can also follow an open-system degassing (exsolved bubbles are decoupled with the melt and outgas from the initial magmatic system).

### 4.1.3. Textural characteristics of the HSA samples

Selected lava and bomb fragments from HSA (Fig. 4c) show similar textures from each other and thus might be representative of similar pre- and syn-eruptive processes. They are characterized by a glassy groundmass hosting microlites, as well as trace occurrences (< 1 vol.%) of fayalite-rich olivine micro-phenocrysts intergrown by titanomagnetites, in accordance with Berthod et al. (2021b) observations. The microlites are composed of acicular laths of alkali feldspar (10-200 μm in length) and skeletal fayalite-rich olivines (5-50 μm) in that order of abundance (Fig. 4c, images 1,2,3, and 4).

The textural characteristics of the microlite population has been used to infer their origins during magma decompression and degassing within the eruptive conduit (c.f., Gurioli et al., 2005; Mastrolorenzo and Pappalardo, 2006; Noguchi et al., 2006). The absence of visible nanolites in these products suggest a better quenching conditions than the FME samples. The vesicularity and crystallinity of lava samples range from 11-13 vol.% and 5-16 vol.%, respectively. DR17_04_02dense (0 vol.% vesicles, 8 vol.% crystals vol.%) and

DR17_04_02vesicular (18 vol.% vesicles, 7 vol.% crystals vol.%) samples are part of the same bomb fragment.

### 4.1.4. Textural characteristics of the LVM samples

Selected samples from LVM (Fig. 4d) are characterized by a glassy microlite-bearing groundmass, with a notable absence of phenocrysts and micro-phenocrysts but containing trace (< 1 vol.%) of crystalline xenoliths, which is a common characteristic of Comorian volcanic products (e.g., Class et al. 1998; Berthod et al., 2021a; Berthod et al. 2021b). The microlites are acicular laths of alkali feldspar (5-100 μm) and skeletal fayalite-rich olivines (5-30 μm) in that order of decreasing abundance (Fig. 4d, images 1,2, and 3).

The sample MAY210721_3b has a vesicularity of 3 vol.% and a crystallinity of 6 vol.%. As noted above, the samples MAY210713_11dense (0 vol.% of vesicles, 8 vol.% of crystals) and MAY210713_11pumice (18 vol.% vesicles, 7 vol.% crystals) are from a single bomb fragment, characterized by intercalation of thin, foliated pumiceous and dense layers (Fig. 4d, image 2), which were separated mechanically prior to STA and EGA-MS analyses. We also note that micro-crystallinity is much more developed in the pumiceous separates than in dense separates (Fig. 4d, image 3), which we interpret to indicate that microlite nucleation and growth were induced by volatile degassing of the pumiceous lava during magma decompression and/or eruption. From SEM-BSE observations, vesicles from the subaerial LVM bombs exhibit coalescence and subsequent fracturing, which yield a highly permeable texture, in contrast with the submarine products.

### 4.2. Volatile distributions and sample behavior upon experimental heating: insights from simultaneous calorimetric, mass evolution and, degassing ($H_2O$, $CO_2$ and, $SO_2$) profiles

STA and EGA-MS analysis undertaken to understand and quantify volatile degassing (Figs. 5 and 6) are interpreted in terms of four major elements. (i) The heat flow (expressed in mW) reflects thermal changes occurring during the heating of each sample. Upon experimental heating the glass transition, degassing, and melting of crystalline phases all appear as endothermic processes (absorbing relaxational or latent heat), whereas crystallization is exothermic (release of latent heat). (ii) The cumulative mass loss (expressed in wt.%) represents the cumulative volatile loss of each sample upon experimental heating, as solely volatile components are able to escape from the crucible. (iii) The mass loss rate (expressed in wt.%/s) is the first-order derivative of the cumulative mass loss and is plotted and analyzed to facilitate the identification of degassing ranges and peak intensities. (iv) The ion current (expressed in nA) represents the simultaneous signal intensities measured for $H_2O$ (m/z = 18), $CO_2$ (m/z = 44) and $SO_2$ (m/z = 64) during sample heating. Note that the ion current background for $H_2O$ is much higher (ca. $4 \times 10^{-1}$ nA) than for $CO_2$ (ca. $8 \times 10^{-4}$ nA) and $SO_2$ (ca. $2 \times 10^{-4}$ nA). Below, systematic correlations are identified between these four data outputs, which we use to interrogate the data and identify the different processes responsible for volatile distribution and degassing as a function of temperature.

Mass loss rate peak values from TGA are compared to $H_2O$ ion current peak intensities from EGA-MS (Fig. 7). A linear correlation is observed for peaks that correspond to $H_2O$ degassing (with negligible degassing of other volatiles). For these specific degassing steps, reliable bulk $H_2O$ contents ($H_2O_{bulk}$) can thus be estimated by measuring the area of the mass loss rate peaks. However, certain other mass loss rate peaks are shifted from this linear correlation, an observation which we take to indicate significant contributions from other volatile species (i.e., $CO_2$, $SO_2$, and/or other unmeasured volatiles). In such cases, $H_2O$, $CO_2$, and/or $SO_2$ distributions cannot be properly distinguished with the TGA signal, even though baseline-corrected EGA-MS ion current intensities can be a proxy of the volatile concentrations

(i.e., ion current intensities are theoretically proportional to the measured volatile concentrations).

From the STA and EGA-MS data, four distinctive physicochemical steps are observed for the studied samples (cf. below).

### 4.2.1. FME samples

The FME phase 1 (Fig. 5a) and FME phase 2 (Fig. 5b) samples both exhibit the same complex features upon experimental heating, which we interpret to be a consequence of their complex textures, including isolated vesicles, melt immiscibility, micro-phenocrysts, as well as microlite- and nanolite-bearing groundmasses.

Step 1 (Figs. 5a and 5b, area 1), from 40 until ca. 500 °C, is interpreted as a relatively low-temperature and diffuse degassing of adsorbed-external $H_2O$ from the samples (c.f., Denton et al. 2012; Giachetti et al., 2015; Biren et al., 2020). This diffuse degassing of adsorbed-external $H_2O$ occurs up to ca. 650 °C. It represents < 0.4 wt.% of the sample masses, which is consistent with their young age and low alteration state minimizing $H_2O$ adsorption. Scattered releases of $CO_2$ are interpreted as the opening and outgassing of pre-existing, isolated, $CO_2$-rich vesicles (< 2 mm - the maximal sample chip length). Small $H_2O$ peaks accompany the main $CO_2$ peaks, indicating mixed $CO_2$-$H_2O$ vesicles, consistent with the observations of Heide et al. (2008) for a 3.3 km b.s.l. Mid-Ocean Ridge Basalt (MORB). These mixed volatile vesicles outgas up to 750 °C. As expected, the most vesicular samples (i.e., samples from the FME phase 1, especially DR12_05_01) exhibit the largest number degassing scattered peaks (representing up to 0.6 wt.% of the sample mass). Based on 17 exploitable baseline-corrected EGA-MS ion current intensities, $CO_2$ fractions in these mixed $CO_2$-$H_2O$ isolated vesicles are 54-95 vol.%. In comparison, Javoy and Pineau (1991) report 95 vol.% $CO_2$ from isolated vesicles in a 3.8 km b.s.l. MORB sample. These observations support the fact that basaltic melts exsolve $CO_2$ dominated bubbles, whereas alkali-rich basanitic melts yield somewhat lower $CO_2$ fractions during volatile exsolution (Dixon, 1997) from ca. 12-14 kbar (i.e., estimated pressure at the main reservoir, Berthod et al., 2021a; mainly exsolution of $CO_2$) to ca. $0.31 \pm 0.02$ kbar (estimated eruptive pressure; exsolution of both $CO_2$ and $H_2O$), consistent with the idea that, due to the relatively low solubility of $CO_2$ relative to $H_2O$, $CO_2$ saturation of ascending magma precedes $H_2O$ saturation.

Step 2 (Figs. 5a and 5b, area 2) corresponds to $T_G$ interval, occurring at ca. 500-600 °C. $T_G$ exhibits a characteristic endothermic event (cf. insets of the heat flow curves in Figs. 5a and 5b). $T_G$ is only detectable here in the relatively glass-rich DR01_01 and DR12_05_01 samples. This step represents the transition to the viscous (liquid) state whence all kinematic data originate.

Step 3 (Figs. 5a and 5b, area 3) corresponds to the main degassing step of the studied samples, which is related to the experimental exsolution of dissolved-magmatic volatiles from the liquid melt. This degassing event occurs above $T_G$ (i.e., in the viscous/liquid regime) at 660-930 °C (peaks at 680-820 °C). This relatively broad range of degassing temperature is interpreted to result from the relatively heterogeneous groundmasses of the samples, yielding different interstitial melt compositions, melt viscosities, and thus volatile exsolution temperatures. The degassing volatile is dominantly $H_2O$, with negligible amounts of $CO_2$ and $SO_2$ (a few ppm). $H_2O_{bulk}$ for this step can be estimated at 0.8-1.0 wt.%, depending on the sample.

Step 4 (Figs. 5a and 5b, area 4) corresponds primarily to quite significant endothermic events (i.e., increase of the heat flow signals), starting from ca. 930 °C and ceasing at the end of the heating experimental segment (i.e., 1300 °C). These events are interpreted as distinct episodes of crystal melting. Nanolite and microlite populations are interpreted to be the first to melt as they were the last to crystallize during eruptive quenching. Due to their relatively low

temperature crystallization in nature and small sizes, they are also thought to melt entirely, representing the main endothermic event of the FME samples, at ca. 930-1130 °C. That temperature range is also associated with a secondary $H_2O$-dominated degassing (together with minor and negligible $CO_2$ and $SO_2$ contents). $H_2O_{bulk}$ for this step is 0.2-0.3 wt.%. In principle, this secondary volatile release may have several origins, linked for example either to the complex nanolite-bearing groundmasses that could trap some nano-sized volatile-bearing melt pockets or to the melting of hydrous apatites and biotites. This degassing could also result from liquid immiscibility, yielding different interstitial melt compositions, melt viscosities, and thus volatile exsolution temperatures. In any event, this secondary $H_2O$ release is considered as part of the dissolved-magmatic $H_2O$ before eruptive quenching and must be added to the main $H_2O_{bulk}$ release in step 3 in order to retrieve a total dissolved-magmatic $H_2O_{bulk}$ which lies then in the range 1.0-1.2 wt.%. In contrast, the scarce micro-phenocrysts melt in a higher temperature range due to their more refractory compositions and larger sizes. All crystal phases are believed to be entirely molten at 1300 °C, as pre-eruptive temperatures for these samples are below this maximum experimental temperature (Berthod et al., 2021a) and because the final endothermic signals tend to equilibrate at the end of each heating segment indicating that all calorimetric events are concluded. Scattered $CO_2$- and $SO_2$-rich signals observed at ca. 1050-1300 °C are interpreted to reflect two distinct processes. One contribution is most likely related to the volatile release of micro-phenocryst-hosted melt/fluid inclusions rich in $CO_2$ and $SO_2$. Interestingly, each FME sample exhibits a variably intense exothermic anomaly at ca. 1150-1200 °C, which are correlated with scattered degassing of $CO_2$ and $SO_2$, and represent up to 0.1 wt.% of mass loss depending on the samples. This late exothermic process is only observed for FME samples and are correlated with the initial degree of liquid immiscibility: samples with mildly pronounce liquid immiscibility (i.e., DR01_05, DR10_02_02t and DR10_05_09t) show relatively slight exothermic anomalies and low mass losses related to the release of $CO_2$ and $SO_2$ compared to the other FME samples which show more developed liquid immiscibility. Thus, we suggest that these simultaneous experimental observations are triggered by the degassing of the remaining volatiles stored in the immiscible liquid droplets (especially the FeS ones), and by the subsequent melt re-homogenization, which theoretically releases energy (exothermic anomalies) during heating (Schuller, 2021).

### 4.2.2. HSA samples

HSA samples (Fig. 6a) show relatively simple features upon experimental heating with respect to the FME samples, presumably because of their relatively simple textures (i.e., isolated vesicles and microlite-bearing but nanolite-free homogeneous groundmasses).

Diffuse degassing of adsorbed-external $H_2O$ starts from step 1 (Fig. 6a, area 1), from 40 to 450 °C for HSA samples. This diffuse degassing of adsorbed-external $H_2O$ occurs until a maximum temperature of ca. 600 °C. In total, adsorbed-external $H_2O$ represents < 0.4 wt.%. This range is similar to that of the FME samples, which suggests that the eruptive ages of these samples are relatively young (cf. Friedman et al., 1997), in agreement with (i) their fresh and unaltered macroscopic aspects, (ii) their occurrence as pyroclastic submarine ejecta from amongst the most recent explosive volcanic vents within the HSA structure, (iii) their origin in the vicinity of the current most vigorously active $CO_2$-rich fluid emissions sites, and (iv) the fact that continuous elevated seismicity is still recorded in the HSA despite the fact that the Fani Maoré eruption has paused or even stopped as of early January 2021 (Rinnert et al., 2020; Foix et al., 2021; Lavayssière et al., 2022; REVOSIMA, 2022). As these samples have relatively low vesicle contents, pre-existing vesicle outgassing is not observed apart from one scattered $H_2O$ degassing peak for the DR02_05_03 sample, revealing the possible occurrence of $H_2O$-rich vesicles in the lava chip samples, coherent with their relatively shallow eruptive emission. Note that a diffuse $CO_2$ degassing is observed for the DR07_01_02b sample at ca. 250-450 °C,

representing 0.3 wt.% of the sample mass and probably reflecting the occurrence of a very small amount of oceanic carbonates in the analyzed sample.

$T_G$ interval is observed in step 2 (Fig. 6a, area 2) at ca. 450-500 °C. Associated endothermic anomalies are clearly visible for all HSA samples (cf. inset of the heat flow curves in Figs. 6a), which is consistent with their crystal-poor nature. Silicate $T_G$ values generally shift upwards in temperature with increasing $SiO_2$ content and downwards in temperature with increasing $H_2O$ content (Dingwell, 1996). The $T_G$ values for the phonolitic HSA samples are lower than the ones for the basanitic FME samples, which is inconsistent with the sample $SiO_2$ and $H_2O$ contents. This shift can be explained by the peralkaline nature of the phonolites.

Exsolution of dissolved-magmatic volatiles from the melt occurs in step 3 (Fig. 6a, area 3), at 600-900 °C. However, degassing peaks are observed within a narrower range of temperatures (650-690 °C) than for the FME samples, consistent with a relatively homogenous interstitial melt composition, and in agreement with the BSE-SEM and Raman spectroscopic observations. The measured volatile species is solely $H_2O$, with $CO_2$ thought to be almost entirely exsolved from the melt at the corresponding eruptive pressure of the HSA samples (i.e., $0.15 \pm 0.02$ kbar) and $SO_2$ concentrations thought to be initially low. Thus, $H_2O_{bulk}$ for this step can be estimated at 0.7-0.9 wt.% for the lava samples and 1.0-1.1 wt.% for the bomb samples.

As HSA samples possess lower crystallinity than FME samples, endothermic anomalies associated with crystal melting are lower in intensity but still noticeable. A first increase in heat flow at ca. 860 °C is interpreted to represent microlite melting. Other increases in heat flow from ca. 1060 °C to 1300 °C, which are interpreted to represent micro-phenocryst melting with synchronous $CO_2$ and $SO_2$ degassing from crystal-hosted fluid or melt inclusions, mainly from the DR07_01_02b sample.

### 4.2.3. LVM samples

LVM samples (Fig. 6b) exhibit a further distinct behavior upon experimental heating, presumably due to their distinct porosity range (i.e., from pumiceous to dense textures). These eruptive samples have been emplaced in subaerial or shallow water conditions and thus exposed to possible subaerial weathering and hydration.

Diffuse degassing of adsorbed-external $H_2O$ starts at step 1 (Fig. 6b, area 1), which ranges from 40 to ca. 500 °C for the LVM samples. This diffuse degassing of adsorbed-external $H_2O$ occurs up to 700 °C, whereby MAY210713_11dense and MAY210713_11pumice separates show the highest adsorbed-external $H_2O$ contents measured in this study (0.6 and 2.3 wt.%). Although inter-connected porosity could play a role in external $H_2O$ adsorption ability, these high values suggest that LVM deposits could be relatively older than the FME and HSA (longer exposure to weathering leading to higher adsorbed-external $H_2O$ content).

$T_G$ interval is observed in step 2 (Fig. 6b, area 2), at ca. 500-550 °C. Associated endothermic anomalies are less visible than for the other samples but are still identifiable (cf. inset of the heat flow curves in Fig. 6b). In this case, $T_G$ values for LVM samples are coherently shifted upwards in temperature compared to $T_G$ values for HSA samples, because LVM and HSA glasses are similar in composition except for the $H_2O$ content that is higher in the HSA glasses than in the LVM ones.

Exsolution of dissolved-magmatic volatiles from the liquid groundmass occurs in step 3 (Fig. 6b, area 3), between ca. 700 and 1000 °C. The measured volatile species is solely $H_2O$, and $CO_2$ is thought to be entirely exsolved from the melt near subaerial pressures (expected maar fragmentation levels) and $SO_2$ concentrations are thought to be initially low. Thus, $H_2O_{bulk}$ for this step can be estimated at 0 wt.% for MAY210713_11pumice sample, 0.3 wt.% for MAY210713_11dense, and 0.1 wt.% for MAY210721_3b. Note that a mass loss of 0.2 wt.% is identifiable for the MAY210713_11pumice sample at ca. 700-1000 °C, which is related to one or more undetermined volatile species.

For all LVM samples, a notable increase in heat flow at ca. 1000-1300 °C is interpreted to represent microlite melting (Fig. 6b, area 4). This increase is even more pronounced for the most crystallized sample (MAY210713_11pumice), consistent with this interpretation. Note that a secondary heat flow increase is visible for the denser samples (MAY210713dense and MAY210721_3b) at ca. 1220 °C, probably reflecting the melting of the rare crystalline xenoliths.

### 4.3. Quantification of dissolved-magmatic $H_2O$ in the interstitial glasses

In order to retrieve the total $H_2O$ content in the interstitial glasses of the samples from STA and EGA-MS analysis ($H_2O_{STA-EGA}$), the total dissolved-magmatic $H_2O_{bulk}$ values must be corrected from the total, vesicularity-corrected, crystal content of each sample.

#### 4.3.1. FME samples

Considering that microlite and nanolite populations are formed during inefficient eruptive quenching, $H_2O_{STA-EGA}$ contents before quenching can be estimated between 1.1 and 1.3 wt.% (Fig. 8): this range is obtained by correcting the total dissolved-magmatic $H_2O_{bulk}$ ranges (1.0-1.2 wt.%) with the 5 vol% pre-existing micro-phenocrysts that formed in the eruptive conduit. This range is lower than the one given by Berthod et al. (2021a) from the crystal-hosted melt inclusions of the FME lavas (1.2-2.3 wt.%). This difference can be explained by the occurrence of partial syn-eruptive $H_2O$ degassing during the magma decompression, as suggested by $H_2O$-bearing vesicles that are outgassed during the previous experimental steps (closed-system degassing), and by large gas plumes released in the ocean column (open-system degassing) at the time of the eruption (Feuillet et al., 2021).

Corrected for total crystallinities of the FME samples (ca. 25-50 vol.%), $H_2O_{STA-EGA}$ contents in the interstitial glasses after eruptive quenching could range from 1.4 to 2.4 wt.%. However, as biotites and apatites are hydrous minerals, some of the $H_2O$ is potentially stored in such microlites and nanolites, which minimizes this range (Fig. 8). All these values nevertheless confirms that a significant part of the pre-eruptive water content was not degassed upon eruption on the sea floor and that $H_2O_{Raman}$ absolute estimations are not reliable when measuring nanolite-bearing groundmasses (Di Muro et al., 2006; Di Genova et al., 2017).

#### 4.3.2. HSA samples

Considering the total crystallinities of the HSA sample (7-16 vol.%), $H_2O_{STA-EGA}$ contents in the interstitial glasses of the two lava samples range from 0.8 to 0.9 wt.%, while $H_2O_{STA-EGA}$ contents in the interstitial glasses of the two bomb samples range from 1.1 to 1.2 wt.%. These values accurately correlate with the $H_2O_{Raman}$ estimations (Fig. 8), which confirms that both methods are reliable when measuring nanolite-free glasses. Slightly higher $H_2O$ contents for the bomb samples might partly explain their explosive behavior compared to the lavas. All these values correspond to $H_2O$ content before and after quenching, as negligible quench crystallization is thought to occur in these products.

#### 4.3.3. LVM samples

Considering the LVM sample crystallinities (4-25 vol.%), $H_2O_{STA-EGA}$ contents in the interstitial glasses range from 0 (for MAY210713_11pumice) to 0.3 wt % (for MAY210713_11dense). These values also correlate well with the $H_2O_{Raman}$ estimations (Fig. 8).

The occurrence of banded pyroclastic bombs exhibiting an intercalation of pumiceous and dense layers of similar chemical composition, has already been described in other eruptive deposits (e.g., Gonnermann and Manga, 2005; Davì et al., 2011; Pistolesi et al., 2015). The data acquired here highlight that the dense and pumiceous parts probably followed different degassing paths in the eruptive conduit, with pumiceous parts exhibiting near-complete $H_2O$ exsolution yielding a high number density of vesicles associated with degassing-induced crystallization, while dense parts do not significantly exsolve $H_2O$ in the upper part of the conduit inhibiting the formation of vesicle and microlites, likely due to magma fragmentation, welding, and subsequent viscous deformation.

## 5. Conclusions and perspectives

The use of STA together with EGA-MS can infer new insights on volcanic samples and ultimately on the associated systems. The present study confirms this approach as a reliable method to identify volatile distribution and contents in volcanic (but also in geological or synthetic) samples, and brings new perspectives to the examination of the samples. The main implications of this work are:

(i) Adsorbed-external $H_2O$ can be clearly distinguished from dissolved-magmatic $H_2O$. This enables the quantitative evaluation of the physical assimilation of external $H_2O$ (e.g., seawater, groundwater, meteoric water). Consistent with their recent age, FME samples do not contain significant adsorbed-external $H_2O$ (< 0.4 wt.%). We note that, undated HSA samples show very similar contents of adsorbed-external $H_2O$ (< 0.4 wt.%), which suggest that these erupted materials are relatively recent as well. On the other hand, LVM samples show different patterns, with higher contents of adsorbed-external $H_2O$ on average. The setup of a new EGA protocol, simultaneously measuring $H_2O$, $CO_2$, $SO_2$ and HCl would eventually lead to further insights into sample composition (Heide et al., 2008) and sample assimilation of hydrothermal fluids or seawater (Kent et al., 1999; Colombier et al., 2019) in order to better mitigate the effect of fluid adsorption through time.

(ii) Pre-existing and isolated vesicles are identifiable, and their volatile compositions can be approximated, in order to bring useful insights into volatile exsolution behavior. Relatively deep FME basanitic lavas have isolated $H_2O$-$CO_2$ vesicles that contain from 54 to 95 vol.% of $CO_2$. These fractionations between $CO_2$ and $H_2O$ during volatile exsolution as a function of pressure and melt composition bring new insights into volatile degassing behavior for the studied magmatic system. Further, the occurrence of $CO_2$-rich vesicles in these products may evidence the formation of $CO_2$-rich fluids at magma reservoir depths, which could accumulate within adjacent porous mushes (Mittal et al., 2022). The interaction between $CO_2$-rich fluids and $H_2O$-rich magmas at depth, known as $CO_2$ flushing, could play a major role in eruptive processes (Métrich et al., 2010; Caricchi et al., 2018).

(iii) $T_G$ is clearly exhibited in glassy-rich samples. This temperature range represents a threshold for the experimental exsolution and analysis of dissolved-magmatic $H_2O$. If the crystal content and crystallization history of the studied samples are known, dissolved-magmatic $H_2O$ in the sample glasses can be accurately quantified, leading to a wide range of dissolved-magmatic $H_2O$ observed here for the eruptive products (1.1-1.3 wt.% for FME, 0.8-1.2 wt.% for HSA, and 0.0-0.3 for LVM). These estimations correlate with $H_2O$ contents estimated by Raman spectroscopic analysis. This technique can also bypass Raman spectroscopic analysis in the analysis of nanolite-bearing glasses. These $H_2O$ contents together with the melt compositions are critical parameters to constrain volatile degassing and melt viscosities. As dissolved-magmatic $H_2O$ decreases melt viscosity (Giordano et al., 2008), we expect that hypothetical dry basanitic compositions (such as those potentially produced in subaerial eruptions) would lead to more viscous and vesicle-rich magmatic mixtures than the

hydrous FME case, which could potentially trigger explosive eruptions (Cashman and Scheu, 2015; Scheu and Dingwell, 2022).

(iv) Finally, the occurrence of liquid immiscibility and associated nanolite growth in the FME basanitic lavas undoubtedly affects the degassing behavior of the studied groundmasses, as shown by the large temperature range of dissolved-magmatic $H_2O$ degassing (i.e., ca. 680-1100 °C), by the uncoherent $T_G$ shift between the nanolite-bearing FME glasses and the nanolite-free HSA and LVM glasses, and by the unexpected exothermic processes occurring between at ca. 1150-1200 °C for FME samples. To gain better insights, a more focused analytical method such as Transmission Electron Microscopy would help to constraint the conditions of formation and the role of the liquid immiscibility as well as the associated nanolite growth on volatile and magma behavior, as nanolites are believed to enhance eruptive explosivity (Cáceres et al., 2020; Di Genova et al., 2020).

# Figures
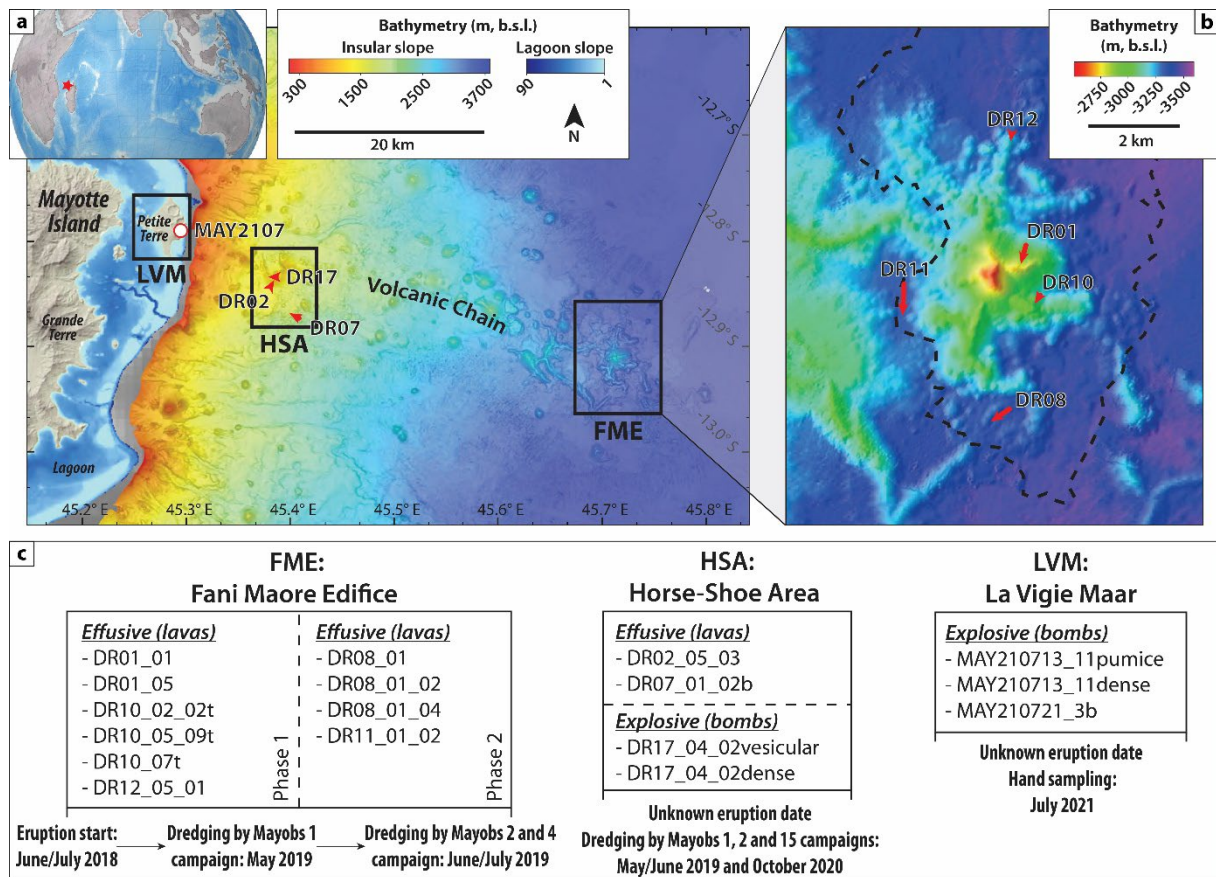


Figure 1 – Main features of the Mayotte active volcanic chain. (a) Location of the Comoros archipelago (red star) and bathymetric map of the eastern slope of Mayotte Island (France), modified from Feuillet et al. (2021). The three black squares delimit the three studied areas, from west to east: La Vigie Maar (LVM) on Petite-Terre Island (Mayotte), the Horse-Shoe Area (HSA), and the Fani Maoré Edifice (FME), with corresponding locations of the studied samples. Red lines show the dredging lines (DR) at FME and HSA, ending arrows indicating their directions. The red and white circle shows the location of hand sampling at LVM. (b) Zoom on the FME area. The black dashed line delimits the new emplaced volcanic material between May 2018 and May 2019 (reflectivity data from Feuillet et al., 2021). (c) List of the samples analyzed in the present study, with eruptive and sampling chronologies. A detailed sample description is available in Table S1.
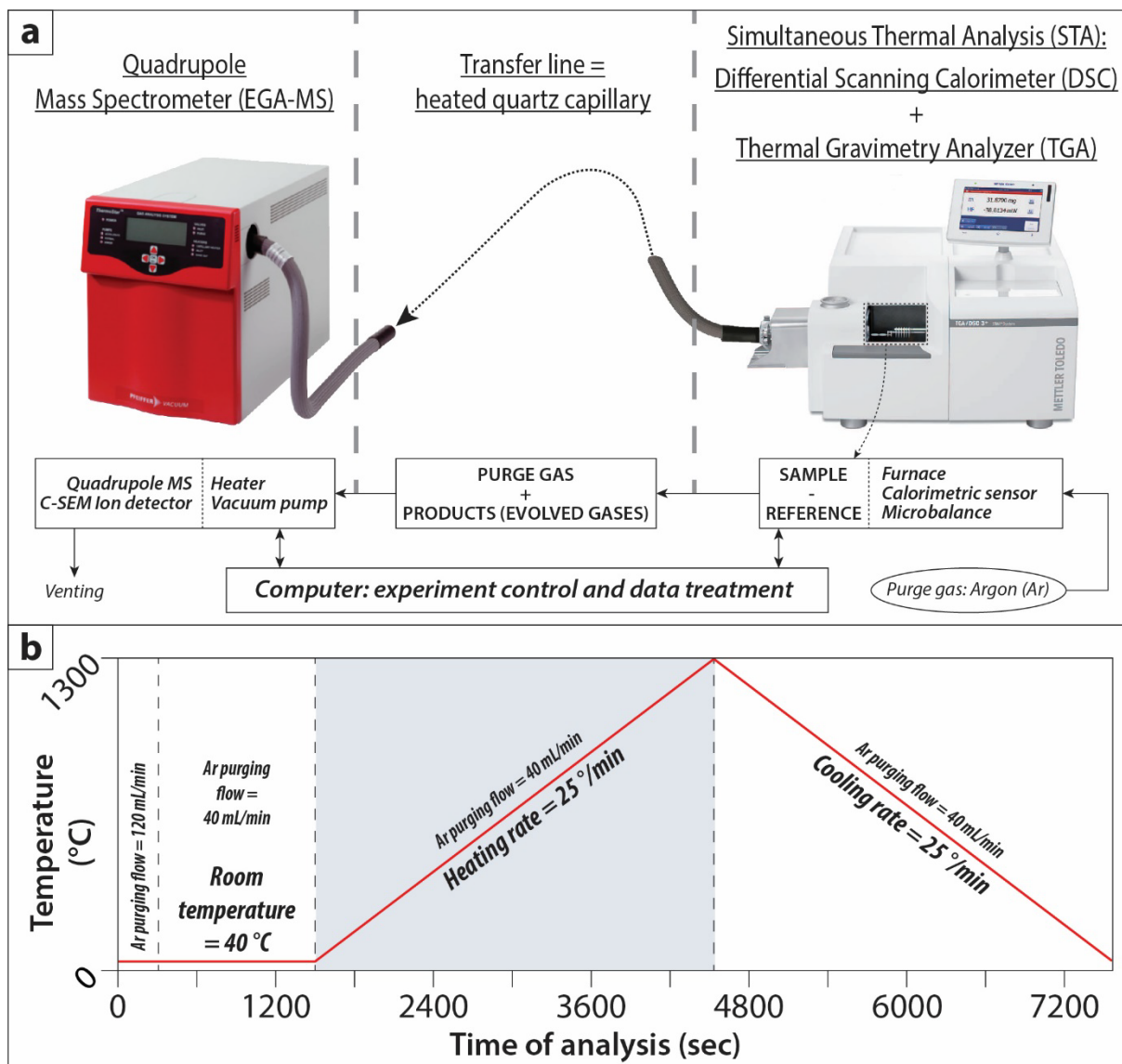
Figure 2 – (a) Instruments and associated analytical procedure used for Simultaneous Thermal Analysis (STA), which includes Differential Scanning Calorimetry (DSC) and Thermal Gravimetry Analysis (TGA), as well as the coupled Evolved Gas Analysis conducted by Mass Spectrometry (EGA-MS). (b) Detailed experimental protocol applied to each studied sample. The results shown in the present study correspond to the signals obtained during the heating segment (grey area).
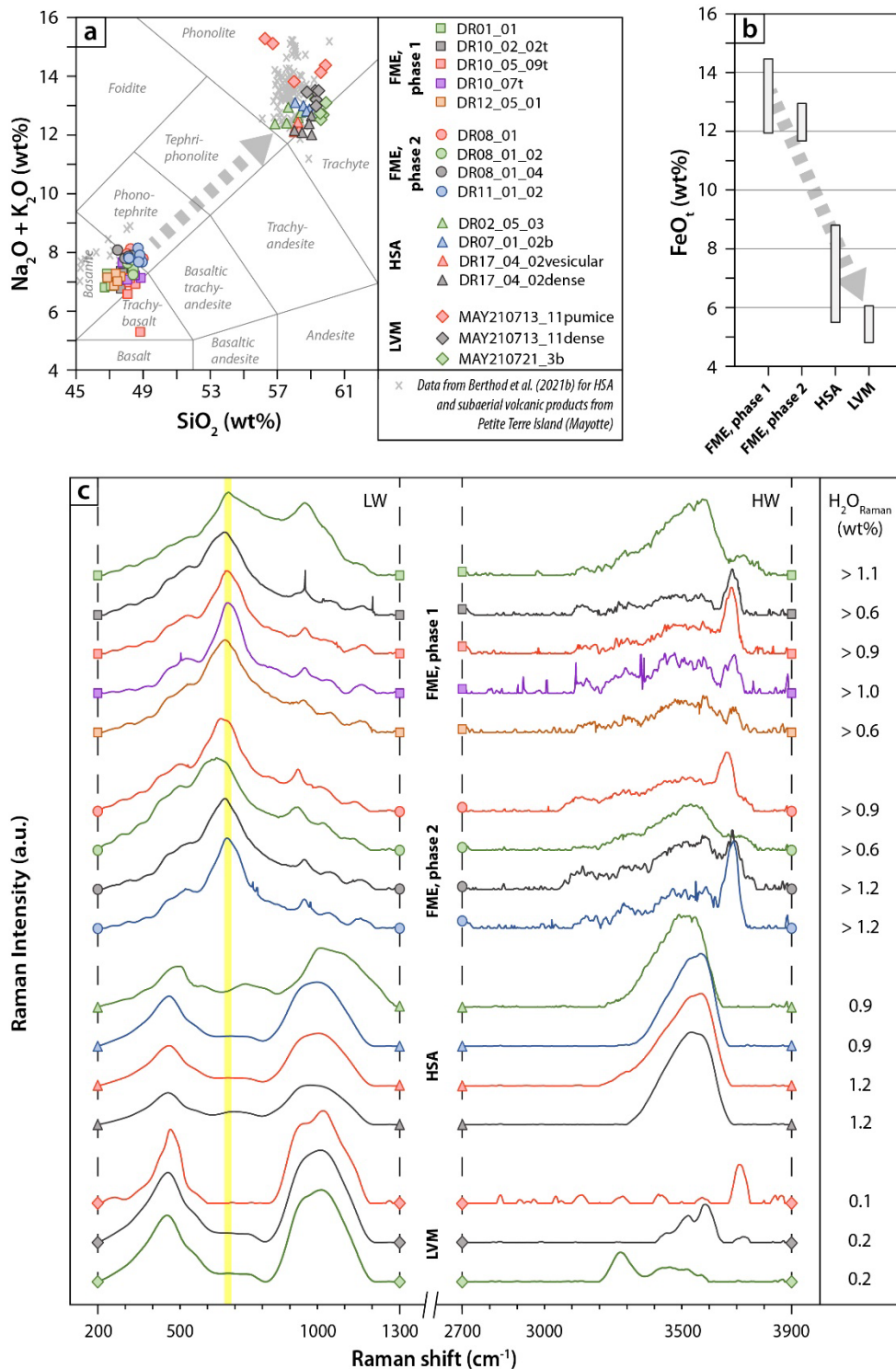
Figure 3 – (a) Groundmass compositions of the investigated samples displayed in a Total Alkali-Silica diagram. (b) Ranges of the total iron content (FeO$_t$) of the corresponding groundmasses. Dashed grey arrows shown in (a) and (b) represent the differentiation trend observed between the sample compositions. Groundmass compositions are detailed in Table S2. (c) Average of the Raman spectra for each studied sample groundmass (both Long's correction and baseline subtraction were applied). The same symbol and color code as in (a) is used. The yellow range shows the Raman peak characteristic of the iron-bearing nanolites, while LW and HW fields represent the silicate and H$_2$O area bands, respectively. Raman analyses are detailed in Table S3. Note that groundmass analysis could not be performed on the DR01_05 sample because of its micro-crystallized texture preventing reproducible analyses within too narrow glass areas (< 10 μm in maximum length).
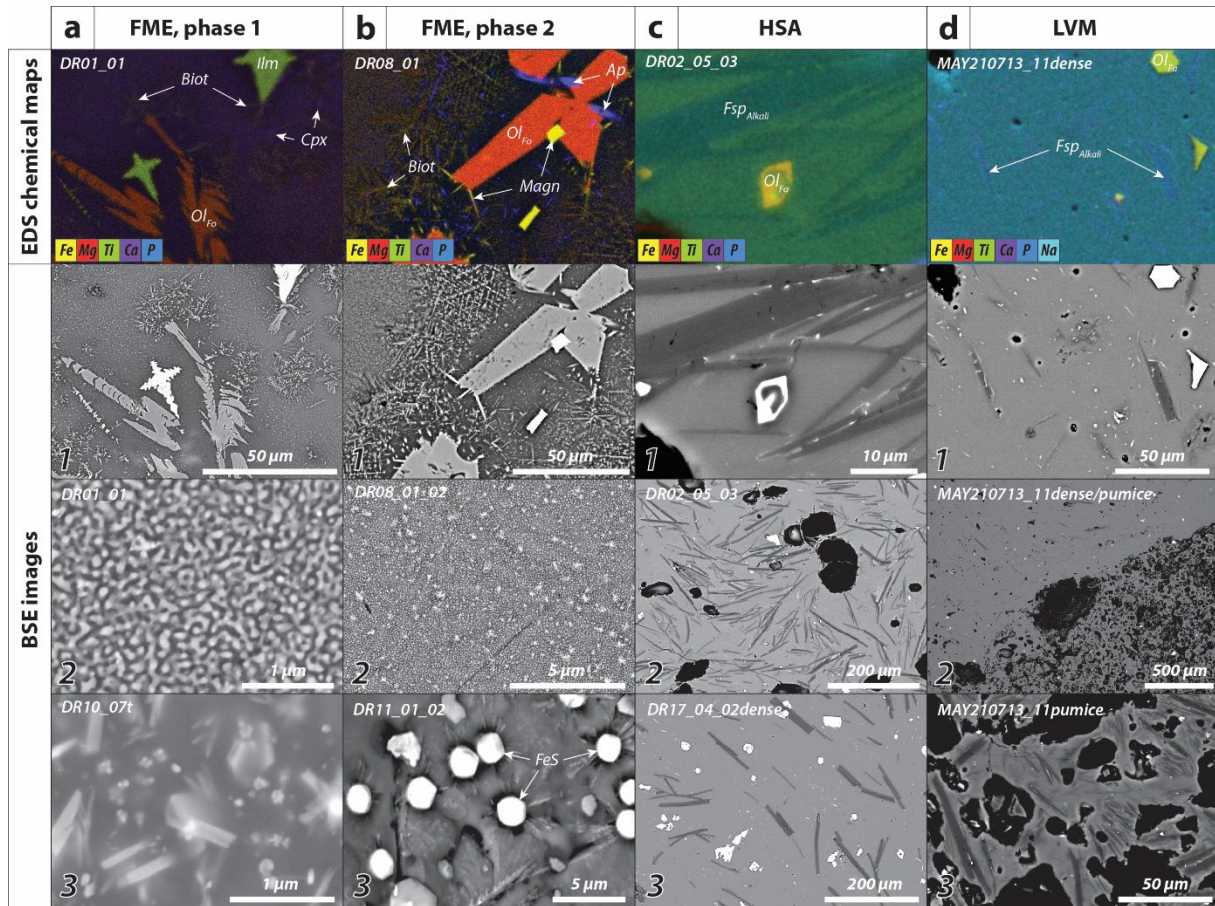
Figure 4 – Representative sample textures from Scanning Electron Microscopy (SEM), with both Energy-Dispersive Spectroscopy (EDS) chemical maps and Back-Scattered Electron (BSE) images. The final colors of EDS maps correspond to the sum of each pre-selected chemical element concentration. Annotated phases correspond to EDS *in-situ* analyses (Ilm: ilmenite; biot: biotite; Cpx: clinopyroxene; $Ol_{Fo}$: forsterite-rich olivine; Ap: apatite; Magn: titanomagnetite; $Fsp_{Alkali}$: alkali-rich feldspar; $Ol_{Fa}$: fayalite-rich olivine). Images from (a) the first and (b) second phase of the Fani Maoré Edifice (FME), (c) the Horse-Shoe Area (HSA), and (d) La Vigie Maar (LVM) samples. The different numbered BSE images are described in the main text. More BSE-SEM images are provided in File S1.
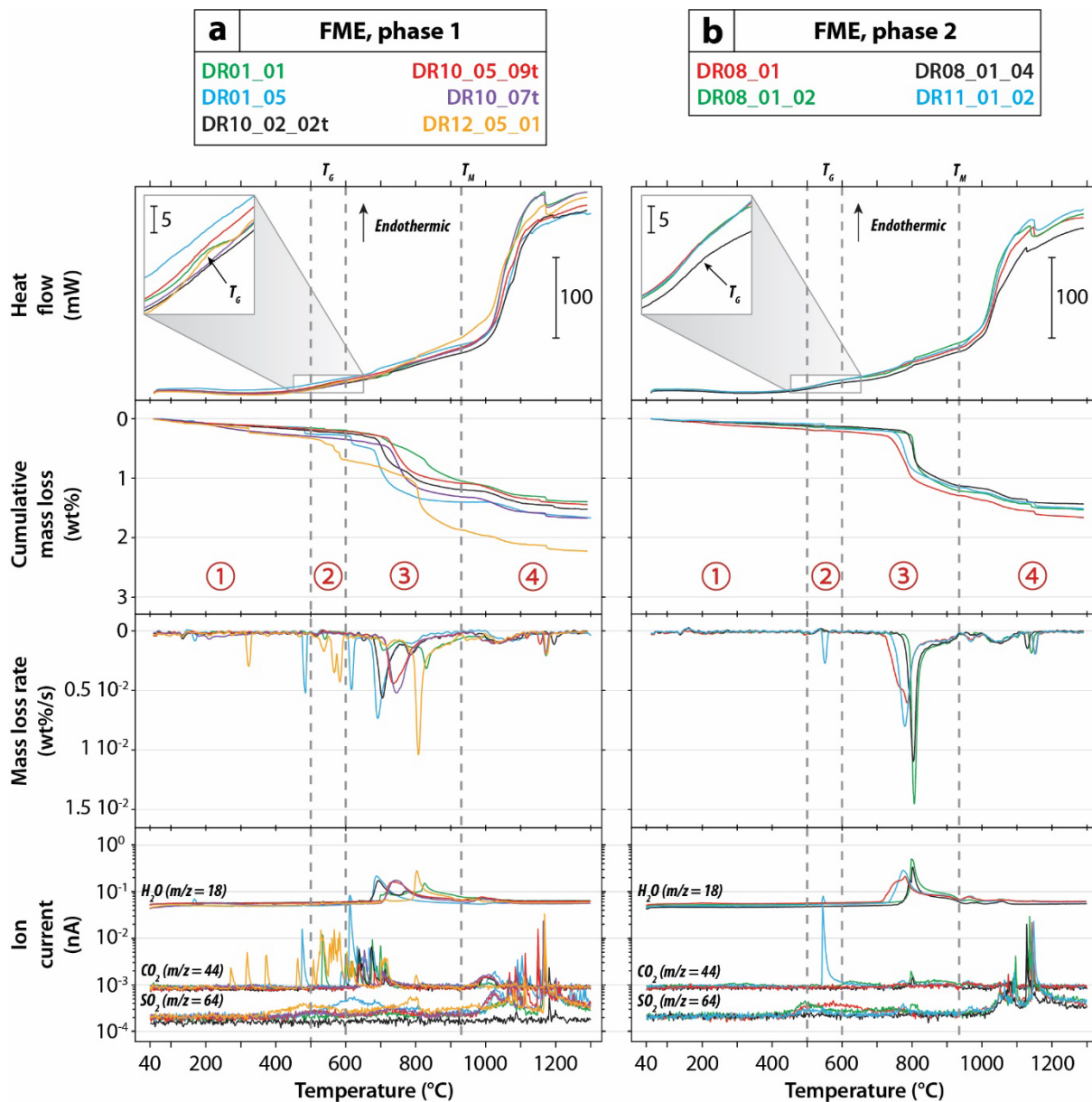
Figure 5 – Simultaneous Thermal Analysis (STA) and synchronous Evolved Gas Analysis conducted by Mass Spectrometry (EGA-MS) performed on the investigated samples from (a) the first and (b) the second phase of the Fani Maoré Edifice (FME). The different graphs represent from top to bottom (i) the Differential Scanning Calorimetry (DSC) raw data expressed as sample heat flow in mW, (ii) the Thermal Gravimetry Analysis (TGA) raw data expressed as sample cumulative mass loss in wt.%, (iii) the derivative of the TGA raw data expressed as sample mass loss rate in wt.%/s and (iv) the Evolved Gas Analysis conducted by Mass Spectrometry (EGA-MS) raw data expressed as ion currents in nA. The different mass-to-charge (m/z) ratios corresponds to $H_2O$ (m/z = 18), $CO_2$ (m/z = 44) and $SO_2$ (m/z = 64). $T_G$ and $T_M$ show estimated glass transition temperature ranges and crystal melting temperatures, respectively. The different numbered temperature steps/events are described in the main text. Detailed STA and EGA-MS data are provided in Table S4.
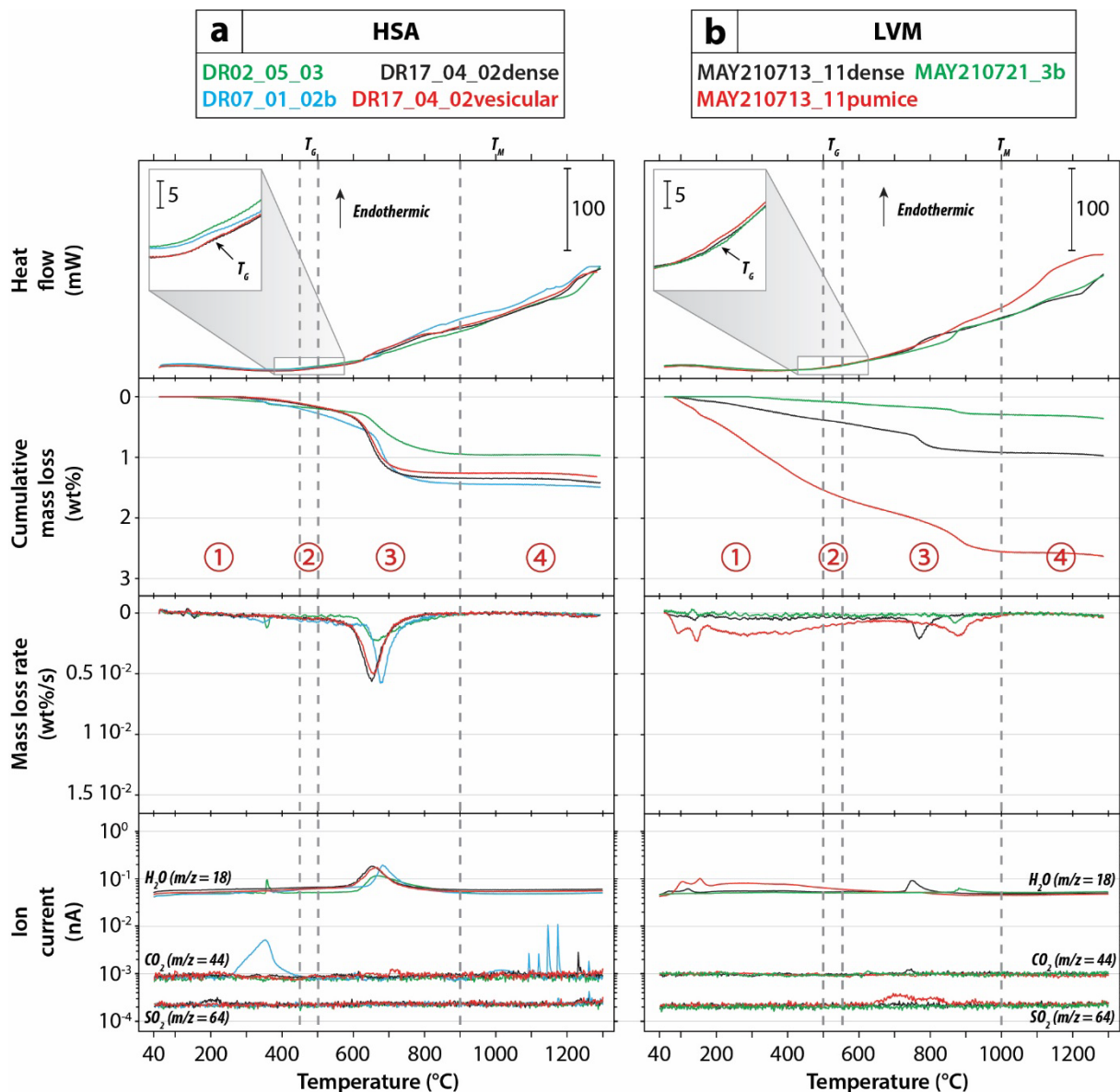
Figure 6 – Simultaneous Thermal Analysis (STA) and synchronous Evolved Gas Analysis conducted by Mass Spectrometry (EGA-MS) performed on the investigated samples from (a) the Horse-Shoe Area (HSA), and (b) La Vigie Maar (LVM). The different graphs represent similar datasets as in Fig. 5. The different numbered temperature steps/events are described in the main text. Detailed STA and EGA-MS data are provided in Table S4.
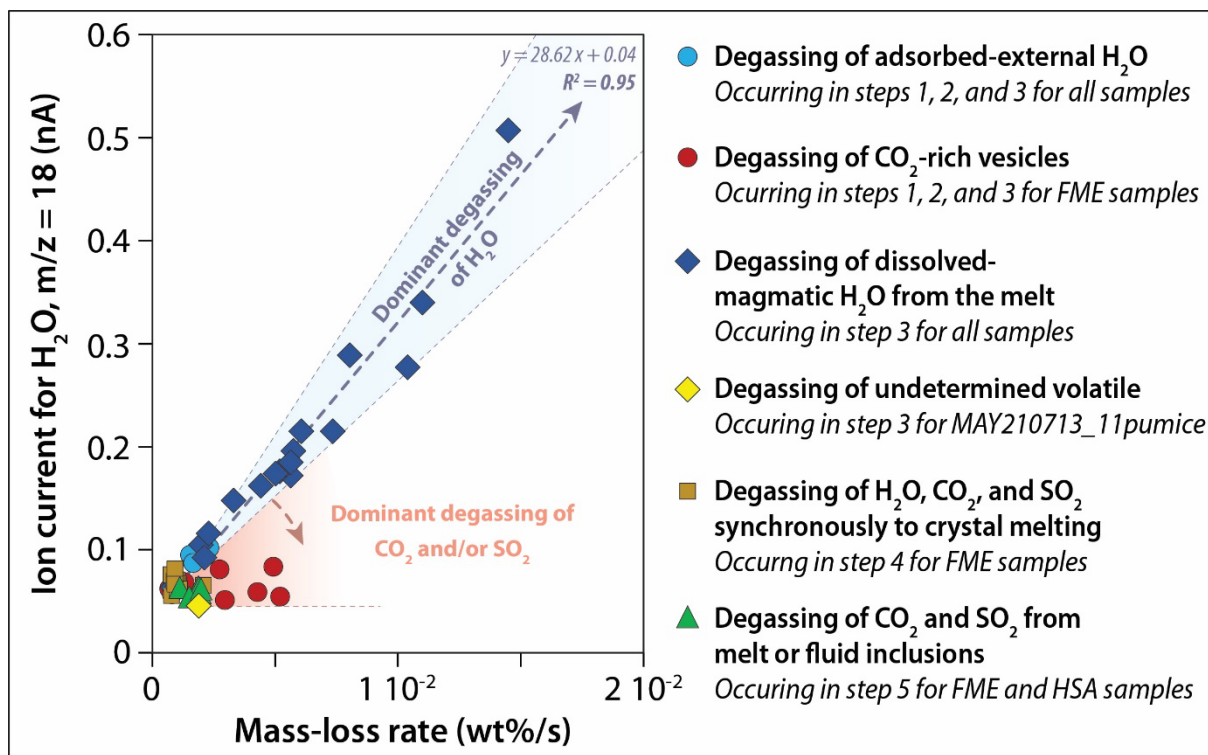
Figure 7 – Mass loss rate peak values from Thermal Gravimetry Analysis (TGA) vs. H₂O ion current peak intensities from Evolved Gas Analysis conducted by Mass Spectrometry (EGA-MS) for all studied samples. Different types of degassing are represented by different symbols and colors. Associated extrapolated data are available in Table S5.
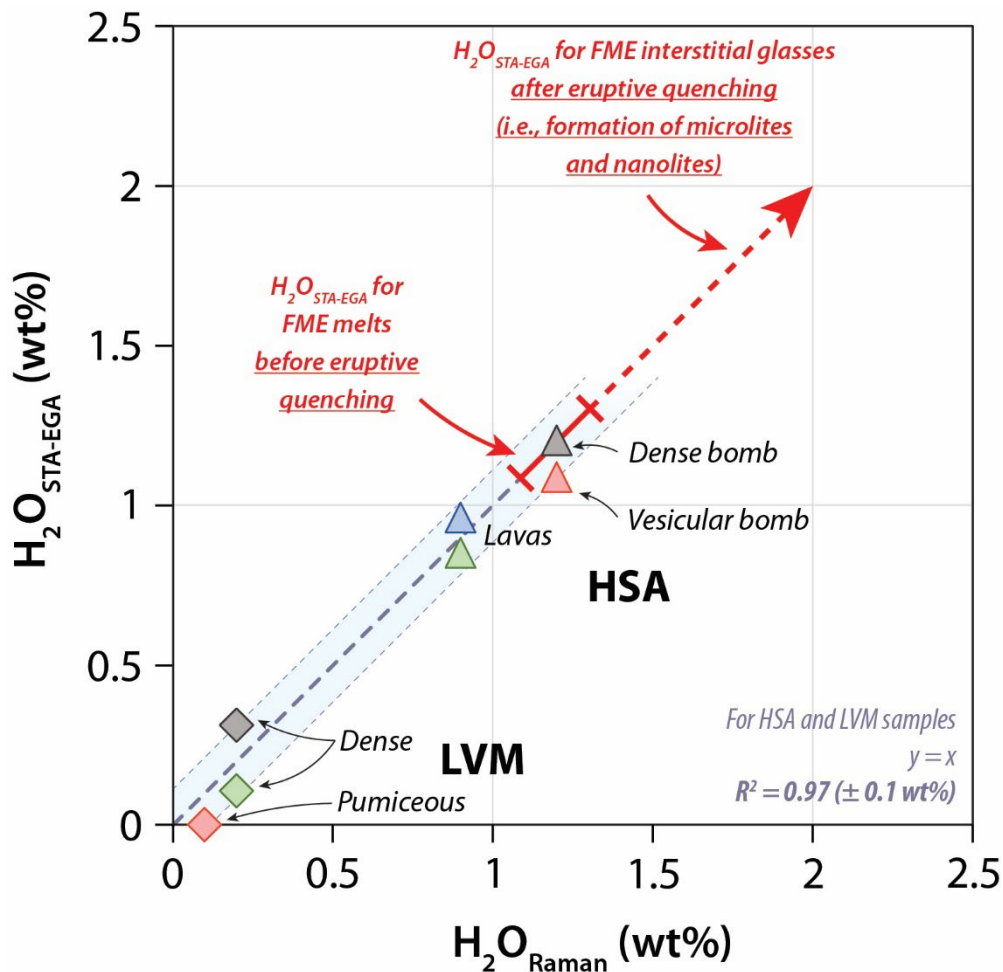
Figure 8 –Dissolved-magmatic $H_2O$ contents estimated from Raman analysis ($H_2O_{Raman}$) vs. sample dissolved-magmatic $H_2O$ contents estimated from Simultaneous Thermal Analysis and synchronous Evolved Gas Analysis conducted by Mass Spectrometry ($H_2O_{STA\text{-}EGA}$). The same symbol and color code as in Figs. 3, 5, and 6 is applied. Associated extrapolated data are available in Table S6.

**Acknowledgments**

# References

Aiuppa, A., Giudice, G., Gurrieri, S., Liuzzo, M., Burton, M., Caltabiano, T., McGonigle, A. J. S., Salerno, G., Shinohara, H., Valenza, M. (2008). Total volatile flux from Mount Etna. Geophysical Research Letters, 35(24), L24302. doi:10.1029/2008gl035871

Applegarth, L. J., Tuffen, H., James, M. R., Pinkerton, H. (2013). Degassing-driven crystallisation in basalts. Earth-Science Reviews, 116, 1-16. doi:10.1016/j.earscirev.2012.10.007

Bachèlery, P., Hémond, C. (2016). Geochemical and Petrological Aspects of Karthala Volcano. In: Active Volcanoes of the Southwest Indian Ocean. Active Volcanoes of the World. Springer, Berlin, Heidelberg. doi:10.1007/978-3-642-31395-0_23

Bachèlery, P., Morin, J., Villeneuve, N., Soulé, H., Nassor, H., Ali, A. R. (2016). Structure and eruptive history of Karthala volcano. In Active Volcanoes of the Southwest Indian Ocean (pp. 345-366). Springer, Berlin, Heidelberg. doi:10.1007/978-3-642-31395-0_22

Berthod, C., Médard, E., Bachèlery, P., Gurioli, L., Di Muro, A., Peltier, A., ... Feuillet, N. (2021a). The 2018-ongoing Mayotte submarine eruption: Magma migration imaged by petrological monitoring. Earth and Planetary Science Letters, 571, 117085. doi:10.1016/j.epsl.2021.117085

Berthod, C., Médard, E., Di Muro, A., Hassen Ali, T., Gurioli, L., Chauvel, C., … Fouquet, Y. (2021b). Mantle xenolith-bearing phonolites and basanites feed the active volcanic ridge of Mayotte (Comoros archipelago, SW Indian Ocean). Contrib Mineral Petrol 176, 75. doi:10.1007/s00410-021-01833-1

Biren, J., Harris, A., Tuffen, H., Chevrel, M. O., Gurioli, L., Vlastélic, I., ... & Calabro, L. (2020). Chemical, Textural and Thermal Analyses of Local Interactions Between Lava Flow and a Tree–Case Study From Pāhoa, Hawai'i. Frontiers in Earth Science, 8, 233. doi:10.3389/feart.2020.00233

Cáceres, F., Scheu, B., Hess, K. U., Cimarelli, C., Vasseur, J., Kaliwoda, M., Dingwell, D. B. (2021). From melt to crystals: The effects of cooling on FeTi oxide nanolites crystallisation and melt polymerisation at oxidising conditions. Chemical Geology, 563, 120057. doi:10.1016/j.chemgeo.2021.120057

Cáceres, F., Wadsworth, F. B., Scheu, B., Colombier, M., Madonna, C., Cimarelli, C., ... Dingwell, D. B. (2020). Can nanolites enhance eruption explosivity? Geology, 48(10), 997-1001. doi:10.1130/G47317.1

Caricchi, L., Sheldrake, T. E., & Blundy, J. (2018). Modulation of magmatic processes by CO2 flushing. Earth and Planetary Science Letters, 491, 160-171. doi:10.1016/j.epsl.2018.03.042

Cashman, K. V., Scheu, B. (2015). Magmatic fragmentation. The encyclopedia of volcanoes (pp. 459-471). doi:10.1016/B978-0-12-385938-9.00025-0

Cashman, K. V. (2004). Volatile controls on magma ascent and eruption. The State of the Planet: Frontiers and Challenges in Geophysics, 150, 109-124. doi:10.1029/150GM10

Cassidy, M., Manga, M., Cashman, K., Bachmann O. (2018). Controls on explosive-effusive volcanic eruption styles. Nature Communications, 9(1), 2839. doi:10.1038/s41467-018-05293-3

Cesca, S., Letort, J., Razafindrakoto, H. N., Heimann, S., Rivalta, E., Isken, M. P., ... Dahm, T. (2020). Drainage of a deep magma reservoir near Mayotte inferred from seismicity and deformation. Nature geoscience, 13(1), 87-93. doi:10.1038/s41561-019-0505-5

Chavrit, D., Humler, E., Morizet, Y., Laporte, D. (2012). Influence of magma ascent rate on carbon dioxide degassing at oceanic ridges: Message in a bubble. Earth and Planetary Science Letters, 357, 376-385. doi:10.1016/j.epsl.2012.09.042

Class, C., Goldstein, S.L., Altherr, R., Bachèlery, P. (1998). The process of plume-lithosphere interactions in the ocean basins: the case of Grande Comore. J. Petrol. 39, 881–903. doi:10.1093/petroj/39.5.881

Coffin, M. F., Rabinowitz, P. D. (1987). Reconstruction of Madagascar and Africa: evidence from the Davie fracture zone and western Somali basin. Journal of Geophysical Research: Solid Earth, 92(B9), 9385-9406. doi:10.1029/JB092iB09p09385

Colombier, M., Vasseur, J., Houghton, B. F., Cáceres, F., Scheu, B., Kueppers, U., ... Dingwell, D. B. (2021). Degassing and gas percolation in basaltic magmas. Earth and Planetary Science Letters, 573, 117134. doi:10.1016/j.epsl.2021.117134

Colombier, M., Mueller, S. B., Kueppers, U., Scheu, B., Delmelle, P., Cimarelli, C., ... & Dingwell, D. B. (2019). Diversity of soluble salt concentrations on volcanic ash aggregates from a variety of eruption types and deposits. Bulletin of Volcanology, 81(7), 1-13. doi:10.1007/s00445-019-1302-0

Davì, M., De Rosa, R., Donato, P., & Sulpizio, R. (2011). The Lami pyroclastic succession (Lipari, Aeolian Islands): a clue for unravelling the eruptive dynamics of the Monte Pilato rhyolitic pumice cone. Journal of Volcanology and Geothermal Research, 201(1-4), 285-300. doi:10.1016/j.jvolgeores.2010.09.010

Denton, J. S., Tuffen, H., & Gilbert, J. S. (2012). Variations in hydration within perlitised rhyolitic lavas—evidence from Torfajökull, Iceland. Journal of Volcanology and Geothermal Research, 223, 64-73. doi:10.1016/j.jvolgeores.2012.02.005

Di Genova, D., Brooker, R. A., Mader, H. M., Drewitt, J. W., Longo, A., Deubener, J., ... Miyajima, N. (2020). In situ observation of nanolite growth in volcanic melt: A driving force for explosive eruptions. Science advances, 6(39), eabb0413. doi:10.1126/sciadv.abb0413

Di Genova, D., Sicola, S., Romano, C., Vona, A., Fanara, S., & Spina, L. (2017). Effect of iron and nanolites on Raman spectra of volcanic glasses: A reassessment of existing strategies to estimate the water content. Chemical Geology, 475, 76-86. doi:10.1016/j.chemgeo.2017.10.035

Di Muro, A., Métrich, N., Allard, P., Aiuppa, A., Burton, M., Galle, B., Staudacher, T. (2016). Magma Degassing at Piton de la Fournaise Volcano. In Active Volcanoes of the Southwest Indian Ocean, Springer, Berlin, Heidelberg. doi:10.1007/978-3-642-31395-0_12

Di Muro, A., Giordano, D., Villemant, B., Montagnac, G., Romano, C. (2006). Influence of composition and thermal history of volcanic glasses on water content determination by microRaman spectrometry. *Applied Geochemistry, 21,* 802-812. doi:10.1016/j.apgeochem.2006.02.009

Di Muro, A., Staudacher, T., Ferrazzini, V., Métrich, N., Besson, P., Garofalo, C., Villemant, B. (2015). Shallow Magma Storage at Piton de la Fournaise Volcano After 2007 Summit Caldera Collapse Tracked in Pele's Hairs. In: American Geophysical Union Monograph vol. 208, pp 189–212. doi:10.1002/97811 18872 079.ch9

Dingwell, D.B., Webb, S.L. (1989). Structural relaxation in silicate melts and non-Newtonian melt rheology in geologic processes. Phys Chem Minerals 16, 508–516. doi:10.1007/BF00197020

Dingwell, D. B. (1996). Volcanic Dilemma--Flow or Blow?. Science, 273(5278), 1054-1055. doi:10.1126/science.273.5278.105

Dixon, J. E. (1997). Degassing of alkalic basalts. American Mineralogist, 82(3-4), 368-378. doi:10.2138/am-1997-3-415

Famin, V., Michon, L., Bourhane, A. (2020). The Comoros archipelago: a right-lateral transform boundary between the Somalia and Lwandle plates. Tectonophysics, 789, 228539. doi:10.1016/j.tecto.2020.228539

Feuillet, N., Jorry, S., Crawford, W. C., Deplus, C., Thinon, I., Jacques, E., ... Van der Woerd, J. (2021). Birth of a large volcanic edifice offshore Mayotte via lithosphere-scale dyke intrusion. Nature Geoscience, 14(10), 787-795. doi:10.1038/s41561-021-00809-x

Feuillet, N. (2019). MAYOBS1 cruise, RV Marion Dufresne. doi:10.17600/18001217

Foix, O., Aiken, C., Saurel, J. M., Feuillet, N., Jorry, S. J., Rinnert, E., Thinon, I. (2021). Offshore Mayotte volcanic plumbing revealed by local passive tomography. Journal of Volcanology and Geothermal Research, 107395. doi:10.1016/j.jvolgeores.2021.107395

Fouquet, Y., Feuillet, N. (2019). MAYOBS4 cruise, RV Marion Dufresne. doi:10.17600/18001238

Friedman, I., Trembour, F.W., Hughes, R.E. (1997). Obsidian Hydration Dating. In: Taylor, R.E., Aitken, M.J. (eds) Chronometric Dating in Archaeology. Advances in Archaeological and Museum Science, vol 2. Springer, Boston, MA. doi:10.1007/978-1-4757-9694-0_10

Giachetti, T., Gonnermann, H. M., Gardner, J. E., Shea, T., & Gouldstone, A. (2015). Discriminating secondary from magmatic water in rhyolitic matrix-glass of volcanic pyroclasts using thermogravimetric analysis. Geochimica et Cosmochimica Acta, 148, 457-476. doi:10.1016/j.gca.2014.10.017

Giordano, D., Russell, J. K., & Dingwell, D. B. (2008). Viscosity of magmatic liquids: a model. Earth and Planetary Science Letters, 271(1-4), 123-134. doi:10.1016/j.epsl.2008.03.038

Giuliani, L., Iezzi, G., Vetere, F., Behrens, H., Mollo, S., Cauti, F., … Scarlato, P. (2020). Evolution of textures, crystal size distributions and growth rates of plagioclase, clinopyroxene

and spinel crystallized at variable cooling rates from a mid-ocean ridge basaltic melt. Earth-Science Reviews, 103165–. doi:10.1016/j.earscirev.2020.103165

Gonnermann, H. M., & Manga, M. (2005). Flow banding in obsidian: A record of evolving textural heterogeneity during magma deformation. Earth and Planetary Science Letters, 236(1-2), 135-147. doi:10.1016/j.epsl.2005.04.031

Gurioli, L., Di Muro, A., Vlastélic, I., Moune, S., Thivet, S., Valer, M., ... & Hénot, J. M. (2018). Integrating field, textural, and geochemical monitoring to track eruption triggers and dynamics: a case study from Piton de la Fournaise. Solid Earth, 9(2), 431-455. doi:10.5194/se-9-431-2018

Gurioli, L., Houghton, B. F., Cashman, K. V., & Cioni, R. (2005). Complex changes in eruption dynamics during the 79 AD eruption of Vesuvius. Bulletin of Volcanology, 67(2), 144-159. doi:10.1007/s00445-004-0368-4

Heide, K., Woermann, E., Ulmer, G. (2008). Volatiles in pillows of the Mid-Ocean-Ridge-Basalt (MORB) and vitreous basaltic rims. Geochemistry, 68(4), 353-368. doi:10.1016/j.chemer.2008.07.001

Hekinian, R., Pineau, F., Shilobreeva, S., Bideau, D., Gracia, E., Javoy, M. (2000). Deep sea explosive activity on the Mid-Atlantic Ridge near 34°50′N: Magma composition, vesicularity and volatile content. Journal of Volcanology and Geothermal Research, 98(1-4), 49–77. doi:10.1016/s0377-0273(99)00190-0

Helo, C., Clague, D. A., Dingwell, D. B., & Stix, J. (2013). High and highly variable cooling rates during pyroclastic eruptions on Axial Seamount, Juan de Fuca Ridge. Journal of Volcanology and Geothermal Research, 253, 54-64. doi:10.1016/j.jvolgeores.2012.12.004

Honour, V. C., Holness, M. B., Charlier, B., Piazolo, S. C., Namur, O., Prosa, T. J., ... & Jean, M. M. (2019). Compositional boundary layers trigger liquid unmixing in a basaltic crystal mush. Nature communications, 10(1), 1-8. doi:10.1038/s41467-019-12694-5

Hotová, G., Slovák, V. (2016). Quantitative TG-MS analysis of evolved gases during the thermal decomposition of carbon containing solids. Thermochimica Acta, 632, 23-28. doi:10.1016/j.tca.2016.03.012

Javoy, M., & Pineau, F. (1991). The volatiles record of a "popping" rock from the Mid-Atlantic Ridge at 14 N: chemical and isotopic composition of gas trapped in the vesicles. Earth and Planetary Science Letters, 107(3-4), 598-611. doi:10.1016/0012-821X(91)90104-P

Jones, M.R., Soule, S.A., Liao, Y., Brodsky, H., Le Roux, V., Klein, F. (2020). Quantitative vesicle analyses and total CO2 reconstruction in mid-ocean ridge basalts. Journal of Volcanology and Geothermal Research, 107109–. doi:10.1016/j.jvolgeores.2020.107109

Jorry, S.J. (2019). MAYOBS2 cruise, RV Marion Dufresne. doi:10.17600/18001222

Kent, A. J., Norman, M. D., Hutcheon, I. D., & Stolper, E. M. (1999). Assimilation of seawater-derived components in an oceanic volcano: evidence from matrix glasses and glass inclusions from Loihi seamount, Hawaii. Chemical Geology, 156(1-4), 299-319. doi:10.1016/S0009-2541(98)00188-0

Kurz, M. D., Jenkins, W. J., Hart, S. R., Clague, D. (1983). Helium isotopic variations in volcanic rocks from Loihi Seamount and the Island of Hawaii. Earth and Planetary Science Letters, 0–406. doi:10.1016/0012-821x(83)90154-1

Lavayssière, A., Crawford, W. C., Saurel, J. M., Satriano, C., Feuillet, N., Jacques, E., & Komorowski, J. C. (2022). A new 1D velocity model and absolute locations image the Mayotte seismo-volcanic region. Journal of Volcanology and Geothermal Research, 421, 107440. doi:10.1016/j.jvolgeores.2021.107440

Leonelli, C., Kamseu, E., Boccaccini, D. N., Melo, U. C., Rizzuti, A., Billong, N., Miselli, P. (2007). Volcanic ash as alternative raw materials for traditional vitrified ceramic products. Advances in Applied Ceramics, 106(3), 135–141. doi:10.1179/174367607x159329

Lemoine, A., Briole, P., Bertil, D., Roullé, A., Foumelis, M., Thinon, I., ... Hoste Colomer, R. (2020). The 2018–2019 seismo-volcanic crisis east of Mayotte, Comoros islands: seismicity and ground deformation markers of an exceptional submarine eruption. Geophysical Journal International, 223(1), 22-44. doi:10.1093/gji/ggaa273

Ligi, M., Bonatti, E., Cipriani, A., Ottolini, L. (2005). Water-rich basalts at mid-ocean-ridge cold spots. Nature, 434(7029), 66–69. doi:10.1038/nature03264

Lipman, P., Banks, N., Rhodes, J. (1985). Degassing-induced crystallization of basaltic magma and effects on lava rheology. Nature 317, 604–607. doi:10.1038/317604a0

Liuzzo, M., Di Muro, A., Rizzo, A. L., Caracausi, A., Grassa, F., Fournier, N., Shafik, B., Boudoire, G., Coltorti, M., Moreira, M., & Italiano, F. (2021). Gas geochemistry at Grande Comore and Mayotte volcanic islands (Comoros archipelago), Indian ocean. Earth and Space Science Open Archive, Journal article DP. doi:10.1002/essoar.10506929.1

Masquelet, C., Leroy, S., Delescluse, M., Chamot-Rooke, N., Thinon, I., Lemoine, A., Franke, D., Watremez, L., Werner, P., Paquet, F., Berthod, C., Cabiativa, V., Sauter, D. The East-Mayotte new volcano in the Comoros archipelago: structure and timing of magmatic phases inferred from seismic reflection data. Submitted to Comptes Rendus Geoscience, Special issue.

Mastrolorenzo, G., & Pappalardo, L. (2006). Magma degassing and crystallization processes during eruptions of high-risk Neapolitan-volcanoes: evidence of common equilibrium rising processes in alkaline magmas. Earth and Planetary Science Letters, 250(1-2), 164-181. doi:10.1016/j.epsl.2006.07.040

Matsumoto, K., & Geshi, N. (2021). Shallow crystallization of eruptive magma inferred from volcanic ash microtextures: a case study of the 2018 eruption of Shinmoedake volcano, Japan. Bulletin of Volcanology, 83(5), 1-14. doi:10.1007/s00445-021-01451-6

McAdam, A. C., Sutter, B., Archer, P. D., Franz, H. B., Wong, G. M., Lewis, J. M., ... & Johnson, S. S. (2020). Constraints on the mineralogy and geochemistry of Vera Rubin ridge, Gale crater, Mars, from Mars Science Laboratory Sample Analysis at Mars evolved gas analyses. Journal of Geophysical Research: Planets, 125(11), e2019JE006309. doi:10.1029/2019JE006309

McIntosh, I. M., Llewellin, E. W., Humphreys, M. C. S., Nichols, A. R. L., Burgisser, A., Schipper, C. I., Larsen, J. F. (2014). Distribution of dissolved water in magmatic glass records growth and resorption of bubbles. Earth and Planetary Science Letters, 401(), 1–11. doi:10.1016/j.epsl.2014.05.037

Metrich, N., Bertagnini, A., Di Muro, A. (2010). Conditions of magma storage, degassing and ascent at Stromboli: new insights into the volcano plumbing system with inferences on the eruptive dynamics. Journal of Petrology, 51, 603-6026. doi:10.1093/petrology/egp083

Michon, L. (2016). The volcanism of the Comoros archipelago integrated at a regional scale. In Active volcanoes of the southwest Indian Ocean (pp. 333-344). Springer, Berlin, Heidelberg. doi:10.1007/978-3-642-31395-0_21

Mittal, T., Jordan, J. S., Retailleau, L., Beauducel, F., & Peltier, A. (2022). Mayotte 2018 eruption likely sourced from a magmatic mush. Earth and Planetary Science Letters, 590, 117566. doi:10.1016/j.epsl.2022.117566

Moore, G. (2008). Interpreting $H_2O$ and $CO_2$ Contents in Melt Inclusions: Constraints from Solubility Experiments and Modeling. Reviews in Mineralogy and Geochemistry, 69(1), 333–362. doi:10.2138/rmg.2008.69.9

Moore, G. (1970). Water Content of Basalt Erupted on the ocean floor. Contribution to Mineralogy and petrology, 28(4), 272–279. doi:10.1007/bf00388949

Mujin, M., Nakamura, M., Miyake, A. (2017). Eruption style and crystal size distributions: Crystallization of groundmass nanolites in the 2011 Shinmoedake eruption. American Mineralogist: Journal of Earth and Planetary Materials, 102(12), 2367-2380. doi:10.2138/am-2017-6052CCBYNCND

Newman, S., & Lowenstern, J. B. (2002). VolatileCalc: a silicate melt–$H_2O$–$CO_2$ solution model written in Visual Basic for excel. Computers & Geosciences, 28(5), 597-604. doi:10.1016/S0098-3004(01)00081-4

Nichols, A. R. L., Potuzak, M., & Dingwell, D. B. (2009). Cooling rates of basaltic hyaloclastites and pillow lava glasses from the HSDP2 drill core. Geochimica et Cosmochimica Acta, 73(4), 1052-1066. doi:10.1016/j.gca.2008.11.023

Noguchi, S., Toramaru, A., & Shimano, T. (2006). Crystallization of microlites and degassing during magma ascent: Constraints on the fluid mechanical behavior of magma during the Tenjo Eruption on Kozu Island, Japan. Bulletin of Volcanology, 68(5), 432-449. doi:10.1007/s00445-005-0019-4

Pistolesi, M., Cioni, R., Bonadonna, C., Elissondo, M., Baumann, V., Bertagnini, A., ... & Francalanci, L. (2015). Complex dynamics of small-moderate volcanic events: the example of the 2011 rhyolitic Cordón Caulle eruption, Chile. Bulletin of Volcanology, 77(1), 1-24. doi:10.1007/s00445-014-0898-3

Potuzak, M., Nichols, A. R., Dingwell, D. B., & Clague, D. A. (2008). Hyperquenched volcanic glass from Loihi seamount, Hawaii. Earth and Planetary Science Letters, 270(1-2), 54-62. doi:10.1016/j.epsl.2008.03.018

Quidelleur, X., Michon, L., Famin, V., Geffray, M. C., Danišík, M., Gardiner, N., Rusquet, A., Zakaria, M. G. (2022). Holocene volcanic activity in Anjouan Island (Comoros archipelago) revealed by new Cassignol-Gillot groundmass K–Ar and 14C ages. Quaternary Geochronology, 67, 101236. 1045. doi:10.1016/j.quageo.2021.101236

REVOSIMA (2022), Bulletin de l'activité sismo-volcanique à Mayotte, Août 2022, IPGP, Université de Paris, OVPF, BRGM, Ifremer, CNRS, www.ipgp.fr/revosima; http://www.ipgp.fr/sites/default/files/ipgp-revosima_bull_20220906.pdf

Rinnert, E., Thinon, I., Feuillet, N. (2020). MAYOBS15 cruise, RV Marion Dufresne. doi:10.17600/18001745

Schipper, C. I., White, J. D., Houghton, B. F. (2010). Syn-and post-fragmentation textures in submarine pyroclasts from Lōihi Seamount, Hawaii. Journal of Volcanology and Geothermal Research, 191(1-2), 93-106. doi:10.1016/j.jvolgeores.2010.01.002

Scheu, B. and Dingwell, D.B. (2022). Magma Fragmentation. Reviews in Mineralogy and Geochemistry 2022, 87 (1), 767–800. doi:10.2138/rmg.2021.87.16

Schöps, D., Schmidt, C. M., & Heide, K. (2005). Quantitative EGA analysis of H2O in silicate glasses. Journal of thermal analysis and calorimetry, 80(3), 749-752. doi:10.1007/s10973-005-0724-4

Schuller, S. (2021). Chapter 4: Phase separation processes in glass. In From glass to crystal: Nucleation, growth and phase separation: from research to applications (pp. 125-154). Les Ulis: EDP Sciences. doi:10.1051/978-2-7598-1997-3.c011

Sharp, T., Stevenson, R. & Dingwell, D. Microlites and "nanolites" in rhyolitic glass: microstructural and chemical characterization. Bull Volcanol 57, 631–640 (1996). doi:10.1007/s004450050116

Song, W., Hess, K. U., Damby, D. E., Wadsworth, F. B., Lavallée, Y., Cimarelli, C., & Dingwell, D. B. (2014). Fusion characteristics of volcanic ash relevant to aviation hazards. Geophysical Research Letters, 41(7), 2326-2333. doi:10.1002/2013GL059182

Szramek, L., Gardner, J. E. Larsen, J. (2006). Degassing and microlite crystallization of basaltic andesite magma erupting at Arenal Volcano, Costa Rica. 157(1-3), 182–201. doi:10.1016/j.jvolgeores.2006.03.039

Thinon, I., Rinnert, E., Feuillet, N. (2021) MAYOBS17 cruise, RV Pourquoi pas ?. doi:10.17600/18001983

Thivet, S., Carlier, J., Gurioli, L., Di Muro, A., Besson, P., Smietana, M., Boudon, G., Bachèlery, P., Eychenne, J., Nedelec, J.-M. (2022). Magmatic and phreatomagmatic contributions on the ash-dominated basaltic eruptions: insights from the April and November-December 2005 paroxysmal events at Karthala volcano, Comoros. Journal of Volcanology and Geothermal Research. 422. doi:10.1016/j.jvolgeores.2022.107500

Thivet, S., Harris, A. J., Gurioli, L., Bani, P., Barnie, T., Bombrun, M., Marchetti, E. (2021). Multi-parametric field experiment links explosive activity and persistent degassing at Stromboli. Frontiers in Earth Science, 9, 431. doi:10.3389/feart.2021.669661

Thivet, S., Gurioli, L., Di Muro, A., Derrien, A., Ferrazzini, V., Gouhier, M., … Arellano, S. (2020a). Evidences of plug pressurization enhancing magma fragmentation during the September 2016 basaltic eruption at Piton de la Fournaise (La Réunion Island, France). Geochemistry, Geophysics, Geosystems, 21(2). doi:10.1029/2019GC008611

Tuffen, H., Owen, J., Denton, J. (2010). Magma degassing during subglacial eruptions and its use to reconstruct palaeo-ice thicknesses. Earth Sci. Rev. 99, 1–18. doi:10.1016/j.earscirev.2010.01.001

Tzevahirtzian, A., Zaragosi, S., Bachèlery, P., Biscara, L., Marchès, E. (2021). Submarine morphology of the Comoros volcanic archipelago. Marine Geology, 432, 106383. doi:10.1016/j.margeo.2020.106383

Veksler, I. V., Dorfman, A. M., Borisov, A. A., Wirth, R., & Dingwell, D. B. (2007). Liquid immiscibility and the evolution of basaltic magma. Journal of Petrology, 48(11), 2187-2210. doi:10.1093/petrology/egm056

Wallace, P. J., Plank, T., Edmonds, M., Hauri, E. H. (2015). Volatiles in magmas. The Encyclopedia of Volcanoes, 163–183. doi:10.1016/B978-0-12-385938-9.00007-9

White, J. D., McPhie, J., Soule, S. A. (2015). Submarine lavas and hyaloclastite. The encyclopedia of volcanoes (pp. 363-375). doi:10.1016/B978-0-12-385938-9.00019-5

Xie, W., Pan, W. P. (2001). Thermal characterization of materials using evolved gas analysis. Journal of Thermal Analysis and Calorimetry, 65(3), 669-685. doi:10.1023/a:1011946707342
Zhang, Y. (1999). A criterion for the fragmentation of bubbly magma based on brittle failure theory. Nature, 402(6762), 648-650. doi:10.1038/45210

Zanotto, E. D., & Mauro, J. C. (2017). The glassy state of matter: Its definition and ultimate fate. Journal of Non-Crystalline Solids, 471, 490-495. doi:10.1016/j.jnoncrysol.2017.05.019

Zhou, W., Van der Voo, R., Peacor, D. R., Zhang, Y. (2000). Variable Ti-content and grain size of titanomagnetite as a function of cooling rate in very young MORB. Earth and Planetary Science, 179(1), 0–20. doi:10.1016/s0012-821x(00)00100-x

Zinke, J., Reijmer, J.J.G., Taviani, M., Dullo, W.-C., Thomassin, B. (2005). Facies and faunal assemblage changes in response to the Holocene transgression in the Lagoon of Mayotte (Comoro Archipelago, SW Indian Ocean). Facies 50, 391–408 (2005). doi:10.1007/s10347-004-0040-7

Zinke, J., Reijmer, J., J., G., Thomassin, B., A., Dullo, W.-C., Grootes, P., M., Erlenkeuser, H. (2003). Postglacial flooding history of Mayotte Lagoon (Comoro Archipelago, southwest Indian Ocean). Marine Geology, 194(3–4), 181–196. doi:10.1016/S0025-3227(02)00705-3